Simulation of KALIF Applied-B Diode Shock-Wave Physics Experiments

J.J. MacFarlane and P. Wang

February 1996

UWFDM-1005

FUSION TECHNOLOGY INSTITUTE

UNIVERSITY OF WISCONSIN

MADISON WISCONSIN

Simulation of KALIF Applied-B Diode Shock-Wave Physics Experiments

J. J. MacFarlane and P. Wang

Fusion Technology Institute
University of Wisconsin-Madison
1500 Engineering Drive
Madison, WI 53706

February 1996

UWFDM-1005

Contents

1. Introduction **1**

2. Calculation of Al Equation of State and Ion Stopping Powers **3**

2.1. Equation of State Models 3

2.2. Calculation of Ion Stopping Powers 9

3. Radiation-Hydrodynamics Simulations **22**

3.1. B_θ-Diode Simulations 22

3.2. Applied-B Diode Simulations 30

4. Summary **42**

1. Introduction

In this report, we describe the results of numerical simulations of shock-wave physics experiments performed at Forschungszentrum Karlsruhe with the KALIF light ion accelerator. In these experiments, intense proton beams with power densities up to ~ 1 TW/cm^2 deposited up to ~ 40 kJ of ion energy in a 6–8 mm diameter [1]. The proton beams with energies $\sim 1.0 - 1.7$ MeV per ion were generated using the "applied B" diode. The beam-target interaction physics was studied by measuring the fluid velocity of the rear surface of Al foils. The velocity measurements were made using an ORVIS-type laser-Doppler velocity diagnostic [1]. Previous analysis of B_θ-diode shock-wave experiments with KALIF have been reported in References [1] through [4].

The generation of shocks in ion beam-heated matter can depend sensitively on: (1) the time-dependent properties of the proton beam; (2) the interaction of the ion beam with the target (i.e., the beam energy deposition profile); and (3) the target equation of state. In addition to comparing the results of our hydrodynamics simulations with experimental shock wave data, we shall also present results showing the sensitivity of the rear surface velocity to a variety of beam and target parameters.

Table 1.1 shows the list of tasks for this study. The primary motivation is to numerically simulate some of the KALIF applied-B diode experiments. However, we have also performed several simulations for B_θ-diode experiments in order to compare with previous work [3,4]. This previous work utilized SESAME equation of state (EOS) tables, as well as a newly-developed analytic EOS.

Table 1.1. Tasks for Shock-Wave Study

1. Analyze shock velocity data obtained in KALIF applied-B diode equation of state experiments.
   (a) compute EOS using hybrid muffin tin/DCA model; compare with SESAME and FZK equations of state;
   (b) perform radiation-hydrodynamics simulations for proton beam-heated targets using EOS models in (a);
   (c) compare simulations to experimental data and assess reliability of EOS models.

Our applied-B diode simulations focused on two types of targets: a 50 μm-thick Al foil; and a 33 μm-thick Al foil backed by a thick ($\gtrsim 1$ mm) transparent LiF substrate. In the latter case, the probe laser propagates freely through the LiF and reflects off the Al rear surface. Radiation-hydrodynamics simulations were performed using both a SESAME EOS model [5] and

our hybrid muffin tin/DCA (detailed configuration accounting) EOS model [6]. In addition, we have compared our EOS predictions with those of SESAME and Goel and Vorobjev [3,4]. This provides an indication of the potential inaccuracies in the simulation results due to uncertainties in the target equation of state.

The structure of this report is as follows. In Section 2, calculated results comparing the three equation of state models are presented. In this section, we also describe stopping power models for Al. In Section 3, results of radiation-hydrodynamics simulations are presented. Here, special attention is paid to the sensitivity of the predictions to both the beam and target properties. Results of this investigation are summarized in Section 4.

2. Calculation of Al Equation of State and Ion Stopping Powers

2.1. Equation of State Models

The temperature and density conditions of the Al targets in the KALIF shock-wave physics experiments span a range of $0 \lesssim T \lesssim 30$ eV and $10^{-1}\,\rho_0 \geq \rho \lesssim \rho_0$, where ρ_0 represents the normal solid density of the material. This can be a very difficult regime for accurately computing equations of state from first principles because of non-ideal effects such as chemical bonding, partial degeneracy, and phase transitions.

The SESAME equation of state tables cover a wide range of plasma conditions, and have been used in previous analyses of KALIF B_θ-diode shock-wave experiments [4]. Goel and Vorobjev [3,4] have also developed a semi-empirical equation of state model for Al for the KALIF experiments. During the past two years, we have developed a hybrid equation of state model for ICF plasmas. In this hybrid EOS model, a detailed configuration accounting (DCA) approach is used for the low-density, high-temperature regime, while a "muffin-tin" model [7] is used for the high-density regime. In order to assess the uncertainties in the EOS modeling, it is useful to make detailed comparisons for the calculated results. In this section, we present results from our hybrid EOS model and compare them with those from SESAME and the Goel and Vorobjev models.

Our hybrid EOS model adopts the usual assumption that electron and ion quantities are additive. With the additive assumption, the Helmholtz free energy per unit mass is:

$$F(\rho, T_e, T_i) = F_i(\rho, T_i) + F_e(\rho, T_e) + F_b(\rho, T_e)\,. \tag{2.1}$$

Here, F_i is the ion free energy calculated from the Cowan ion EOS model [8], which reduces to the ion ideal gas limit at high temperatures and to the Debye-Gruneisen law [9] in the solid phase. The quantity F_e is the electron free energy obtained from the DCA ionization equilibrium calculation at low densities and from the muffin-tin model at intermediate and high densities. Finally, F_b is a semi-empirical correction for chemical bonding effects in the solid state.

The pressure (P), entropy (S), and energy (E) can be obtained from the free energy from the following equations:

$$\begin{aligned}
p_e &= \rho^2 \tfrac{\partial F_e}{\partial \rho}\,, \qquad S_e = -\tfrac{\partial F_e}{\partial T_e}\,, \qquad E_e = F_e + T_e S_e\,, \\
p_i &= \rho^2 \tfrac{\partial F_i}{\partial \rho}\,, \qquad S_i = -\tfrac{\partial F_i}{\partial T_e}\,, \qquad E_i = F_i + T_i S_i\,, \\
p_b &= \rho^2 \tfrac{\partial F_b}{\partial \rho}\,, \qquad S_b = -\tfrac{\partial F_b}{\partial T_e}\,, \qquad E_b = F_b + T_b S_b\,.
\end{aligned} \tag{2.2}$$

In order to see how the model works it is important to understand which terms make the major contributions. For material with large atomic number at high temperature, most of the pressure comes from free electrons and the key variable is the ionization state. Our

DCA ionization equilibrium calculations, based on Hartree-Fock atomic data, provide accurate ionization distributions for high temperature, low density plasmas. In intermediate- and high-density regimes, the muffin-tin model gives a reasonably accurate representation of free electron contributions with the inclusion of effects associated with quantum shell structure in the ionization potentials. At very high densities the free electrons are degenerate and produce a large pressure independent of temperature; this effect is well reproduced by the muffin-tin model.

Even though the muffin-tin model represents a significant improvement over the spherical-cell Thomas-Fermi theory [9], there can still be large inaccuracies near the cold solid regime ($\rho = \rho_0$, $T \simeq 0$). In this case, the muffin-tin model predicts a mult-kbar pressure compare to a multi-megabar pressure predicted by Thomas-Fermi (TF) theory; while in reality chemical bonds support a finite matter density at zero total pressure. In order to correct this discrepancy we add a semi-empirical bonding correction to the energy:

$$F_b = E_b = E_0\{1 - \exp(b\,[1 - (\rho_0/\rho)^{1/3}])\}\,, \tag{2.3}$$

where ρ_0 is the normal solid density, and E_0 and b are positive numbers which characterize the bond strength and range. The energy $E_b(\rho)$ is a constant ($\simeq E_0 > 0$) at very low density, is zero at solid density, and becomes constant again ($\simeq -E_0[\exp(b) - 1]$) at high density. The convenient functional form of this correction was first introduced by Barnes [10] on the basis of its similarity to the attractive term in the well-known Morse potential.

The bonding correction to the pressure can be obtained from:

$$p_b = \rho^2 \frac{\partial F_i}{\partial \rho} = -\left(\frac{E_0\, b\, \rho_0}{3}\right)\left(\frac{\rho}{\rho_0}\right)^{2/3} \exp\left(b\left[1 - \left(\frac{\rho_0}{\rho}\right)^{1/3}\right]\right)\,. \tag{2.4}$$

The parameters E_0 and b are determined by requiring that the total pressure and bulk modulus be correct for the initial cold solid. The experimental bulk modulus is required to be:

$$B = \rho\left(\frac{\partial p_{\rm tot}}{\partial \rho}\right)_{\rho_0} = \rho\left(\frac{\partial p_e}{\partial \rho} + \frac{\partial p_i}{\partial \rho}\right)_{\rho_0} - (b+2)\,\frac{E_0\, b\, \rho_0}{9}\,. \tag{2.5}$$

This equation, together with the requirement that

$$p_{\rm tot}(\rho_0, 0) = 0\,,$$

determine E_0 and b. With the correct bulk modulus, this correction can dramatically improve the zero temperature equation of state as shown in Figure 2.1. In Figure 2.2, we show a comparison of the calculated aluminum shock Hugoniot with experimental data [11]. It can be seen that very good agreement is achieved. In Table 2.1, we list the bulk modulus values [10] for several materials.

Ions make a large contribution to pressure for low temperatures and low densities where one has a neutral atomic gas, and also near the solid density. At higher density and/or higher

Table 2.1. The Bulk Modulus of Several Materials

Element	V_0 (cm^3/g)	B_0 (Mbar)
Be	0.5420	1.14
Al	0.3591	0.763
Ti	0.2219	1.07
Ni	0.1124	1.90
Cu	0.1121	1.37
Mo	0.0980	2.69
W	0.0522	3.08
Pb	0.0882	0.447

temperature, the ion pressure is usually much less than the electron pressure. For typical target conditions of the KALIF beam-target interaction experiments, ion contributions can be very important. Instead of using an ideal gas model to approximate the ion contribution, we have used the more sophisticated Cowan model [8] for ion equation of state calculations.

The Cowan model constructs thermodynamic functions in terms of a known melting temperature $T_m(\rho)$ and Debye temperature $\Theta_D(\rho)$ which are assumed to obey the Lindemann melting law [12]:

$$T_m(\rho)/\Theta_D^2(\rho) = \alpha/\rho^{2/3}\,. \tag{2.6}$$

One can define the scaling variables u and w as

$$\begin{aligned} u &= \Theta_D(\rho)/T\,, \\ w &= T_m(\rho)/T\,. \end{aligned}$$

Then the solid phase corresponds to the range $w > 1$, and the fluid phase corresponds to the range $w < 1$.

The ion free energy per gram is written as

$$F_i(\rho, T) = (kT/AM_p) f(u, w)\,, \tag{2.7}$$

where AM_p is the mass of the ion, and the function $f(u, w)$ is defined as:

$$\begin{aligned} f &= -8 + 7w^{0.214} + \frac{3}{2}\log\left(\frac{u^2}{w}\right)\,,\ w < 1 \qquad \text{(fluid phase)} \\ f &= -1 + 3\log u + \left(\frac{3u^2}{40} - \frac{u^4}{2240}\right)\,,\ w > 1,\ u < 3 \qquad \text{(high-T solid)} \\ f &= \frac{9}{8}\,u + 3\log(1 - e^{-u}) - \frac{\pi^4}{5u^3} + e^{-u}\left(3 + \frac{9}{u} + \frac{18}{u^2} + \frac{18}{u^3}\right)\,,\ w > 1\,,\ u > 3 \ \text{(low-T solid)}\,. \end{aligned}$$

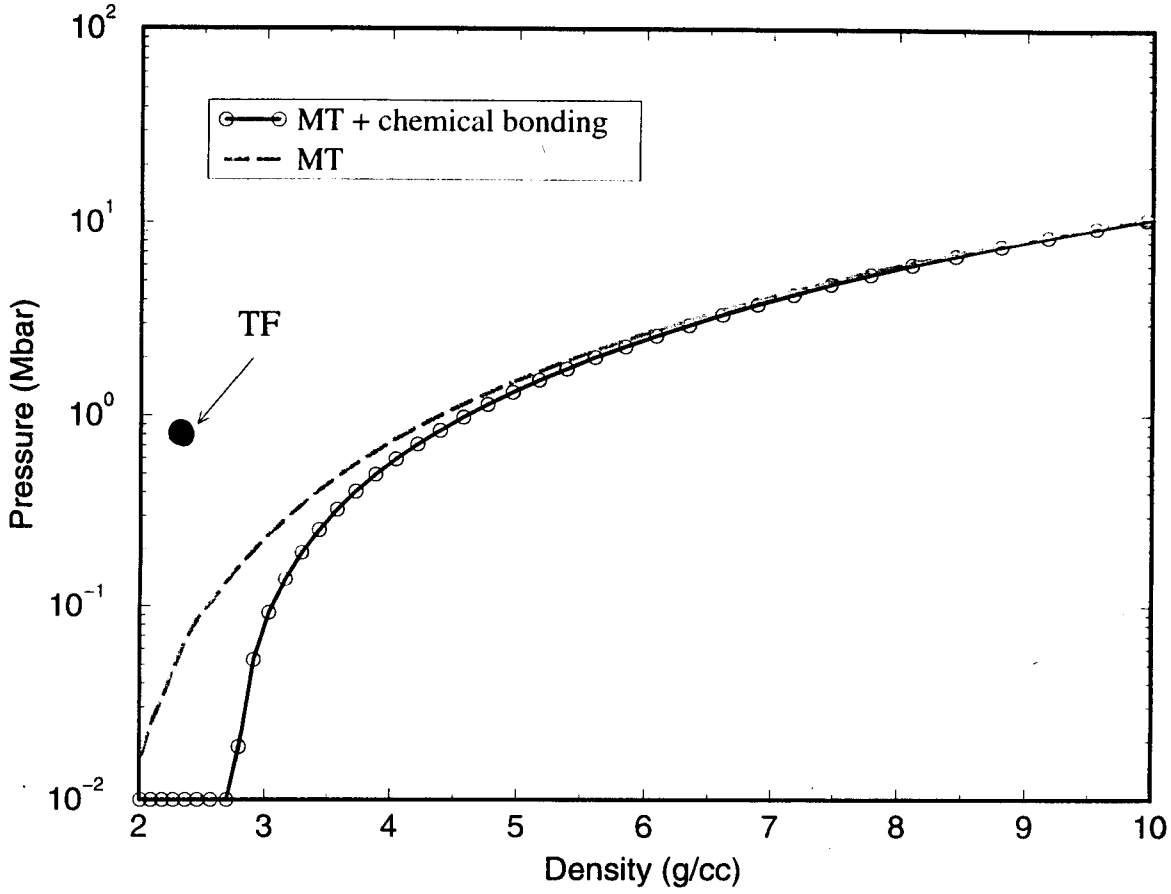

Figure 2.1. Aluminum zero temperature equation of state. The dashed curve represents the muffin-tin calculation. The solid curve shows the result with the chemical bonding correction. The accurate pressure at $\rho = 2.7$ g/cc is zero. The dot indicates the Thomas-Fermi value at a particular density point.

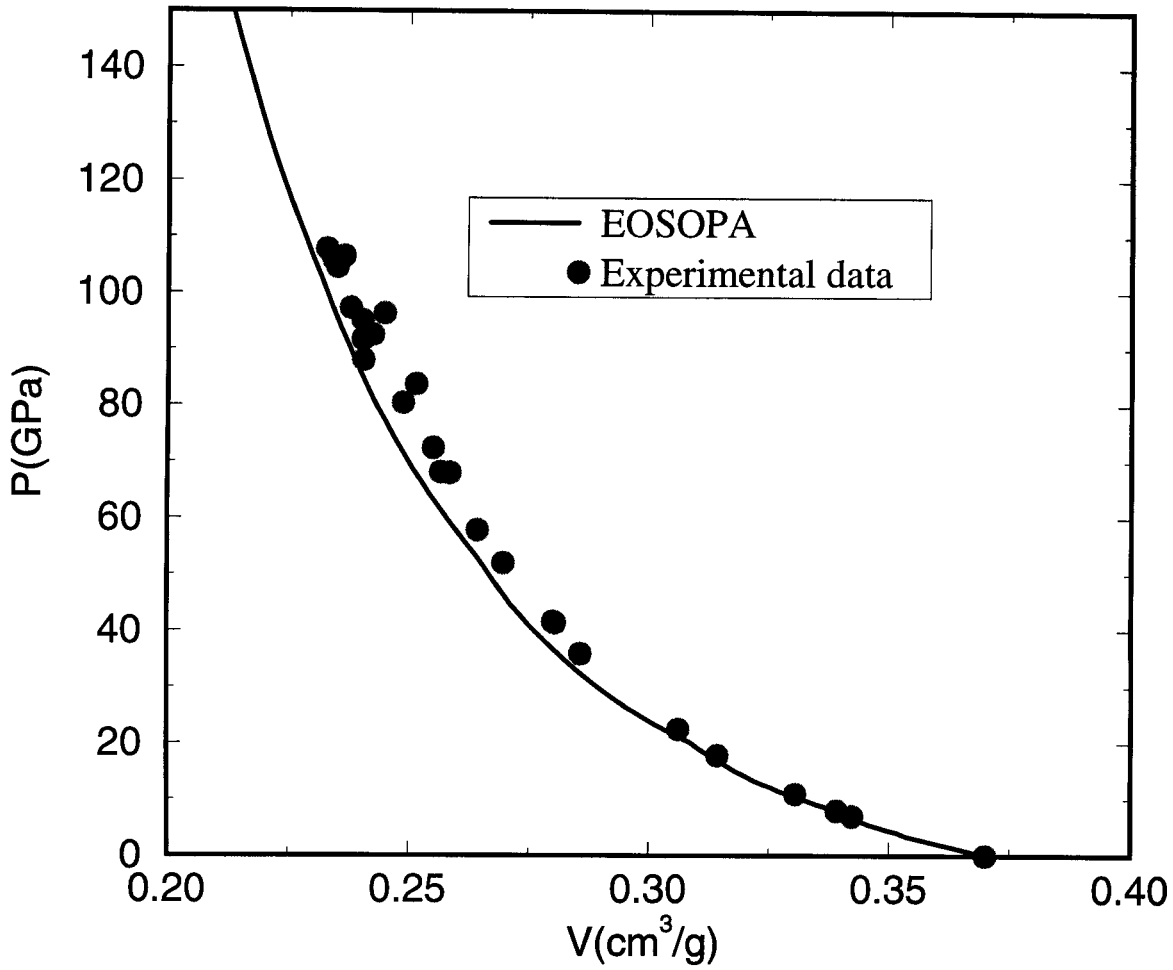

Figure 2.2. Comparison of calculated shock Hugoniot for aluminum with experimental data [11].

From the equations given above, the solid-phase ion pressure and energy are:

$$p_i = \rho^2 \frac{\partial F_1}{\partial \rho} = \frac{\rho^2}{AM_p} f'(u) \frac{\Theta_D}{\partial \rho} \tag{2.8}$$

$$E_i = -T^2 \frac{\partial}{\partial T} \left(\frac{F_i}{T} \right) = \frac{\Theta_D}{AM_p} f'(u) \,. \tag{2.9}$$

With the use of the Gruneisen coefficient

$$\gamma_s = \frac{\partial \log \Theta_D}{\partial \log \rho} \,, \tag{2.10}$$

we have

$$p_i = \gamma_s(\rho) \rho E_i \,.$$

The fluid-phase energy and pressure are:

$$E_i = \left(\frac{T}{AM_p} \right) \left(\frac{3}{2} + \frac{3}{2} w^{0.214} \right)$$

$$p_i = \left(\frac{\rho T}{AM_p} \right) \left[1 + w^{0.214} (3\gamma_s - 1) \right] \,.$$

The Cowan model also provides formulae for the calculation of the melting temperature T_m, the Debye temperature Θ_D, and the solid-phase Gruneisen coefficient γ_s which are listed as following:

$$T_m = 0.32 \left[\frac{\xi^{2b+10/3}}{(1+\xi)^4} \right] \text{ (eV)}$$

$$\Theta_D = \left[\frac{1.68}{(Z+22)} \right] \left[\frac{\xi^{b+2}}{(1+\xi)^2} \right] \text{ (eV)}$$

$$\gamma_s = \frac{b+2}{(1+\xi)}$$

$$b = 0.6\, Z^{1/9} \,, \qquad \xi = \frac{\rho}{(A/9Z^{0.3})} \,.$$

It is important to note that the Cowan ion EOS model automatically reduces to the well-known limiting cases of: (1) the ideal gas law, (2) the fluid scaling law, (3) the Lindemann melting law, (4) the Dulong-Petit law, and (5) the Gruneisen pressure law.

The hybrid EOS model is designed to provide reliable equations of state over a wide range of material conditions. Figure 2.3 shows the results for energy and pressure isotherms for aluminum calculated using our hybrid model. In the low-density regime, the nonlinear behavior due to atomic internal excitation/ionization is clearly seen. The cohesive, degenerate, and the pressure ionization effects are observed for the low-temperature, high-density regime.

Comparisons of our calculated pressure isotherms for aluminum at several different temperatures relevant to the KALIF beam-target interaction experiments are presented in Figures 2.4 through 2.8. Comparisons with the EOS of Goel and Vorobjev, Bushman, and SESAME are also shown at the bottom of Figures 2.6 through 2.8.

For the case of $T = 0$, our calculated results agree very well with the SESAME data (Figure 2.4). For temperatures of $T = 0.1$ eV (Figure 2.5), differences of tens of percent appear between our results and the SESAME data in the regime near solid density. At $T = 2.5$ eV and $\rho \simeq 0.5\,\rho_0$, our calculated pressure is about 40 percent higher than the SESAME pressure. As the temperature increases, the differences become smaller. We have found that the main source for these discrepancies comes from the ion contribution equation of state. The largest differences appear in the strong coupling plasma regime where approximations used by different models can lead to large uncertainties. At relatively high temperatures and/or densities, our results are in good agreement with the SESAME data.

The plots at the bottom of Figures 2.6–2.8 were taken from Goel and Vorobjev [3]. (Note that the temperatures are slightly different than those used in the EOSOPA/SESAME comparisons in the upper portion of the figures.) A critical regime for the KALIF shock-wave experiments is $T \sim 1 - 10$ eV and $\rho/\rho_0 \sim 10^{-1} - 1$. At $\rho \simeq 0.5\,\rho_0$, the EOSOPA pressures are about 40% and 20% higher than SESAME at temperatures of 2.5 eV and 10 eV, respectively. By comparison, Figure 2.6 shows that Goel and Vorobjev pressures at $T = 9$ eV and 17 eV are a factor of 1.6 and 1.8 lower than SESAME. Thus, we can expect differences between the EOSOPA and Goel and Vorobjev pressures to be approximately a factor of 2 in this critical regime for the KALIF shock-wave experiments.

2.2. Calculation of Ion Stopping Powers

Ion stopping powers have been calculated with the use of a unified self-consistent field model [13]. This model includes a realistic treatment of the electron density distribution of an atom embedded in a plasma, as well as a full random phase approximation stopping number [14] which extrapolates the zero temperature Lindhard stopping number to arbitrary temperatures. Therefore, it can accommodate a wide range of temperatures and densities relevant to ICF plasmas. Figure 2.9 shows a comparison of our calculated proton stopping powers in cold aluminum and gold targets with experiment. It can be seen that in both cases the agreement is very good, indicating that our stopping power model should provide accurate ion stopping powers in cold materials for both low-Z and high-Z targets.

For finite temperature plasmas, the model accounts for the stopping effects due to electrons in ground states, excited states and continuum states in a self-consistent manner. In this way, the ion stopping power in targets of arbitrary plasma conditions can be calculated within a single unified model.

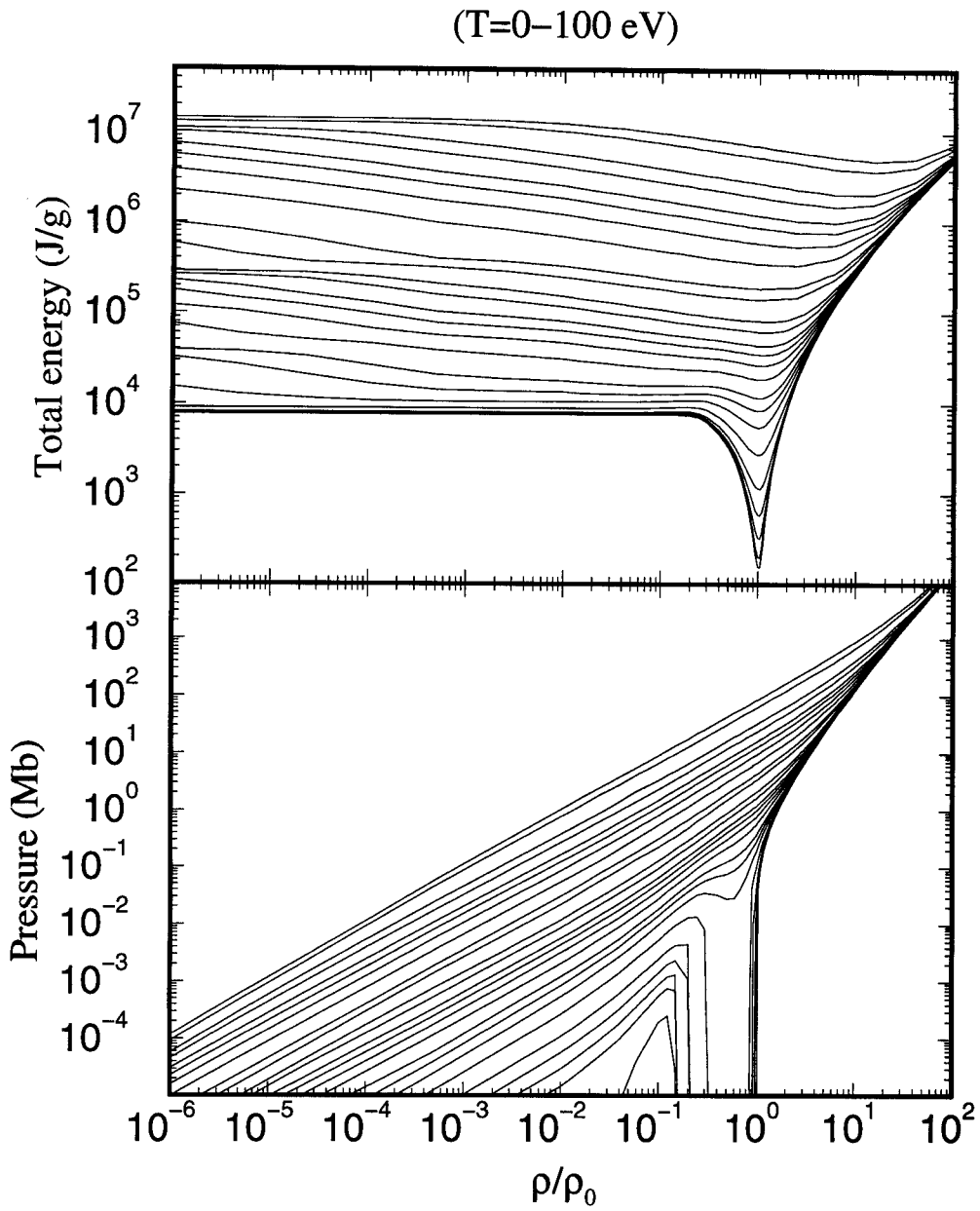

Figure 2.3. Energy and pressure isotherms for Al calculated using the EOSOPA hybrid EOS model.

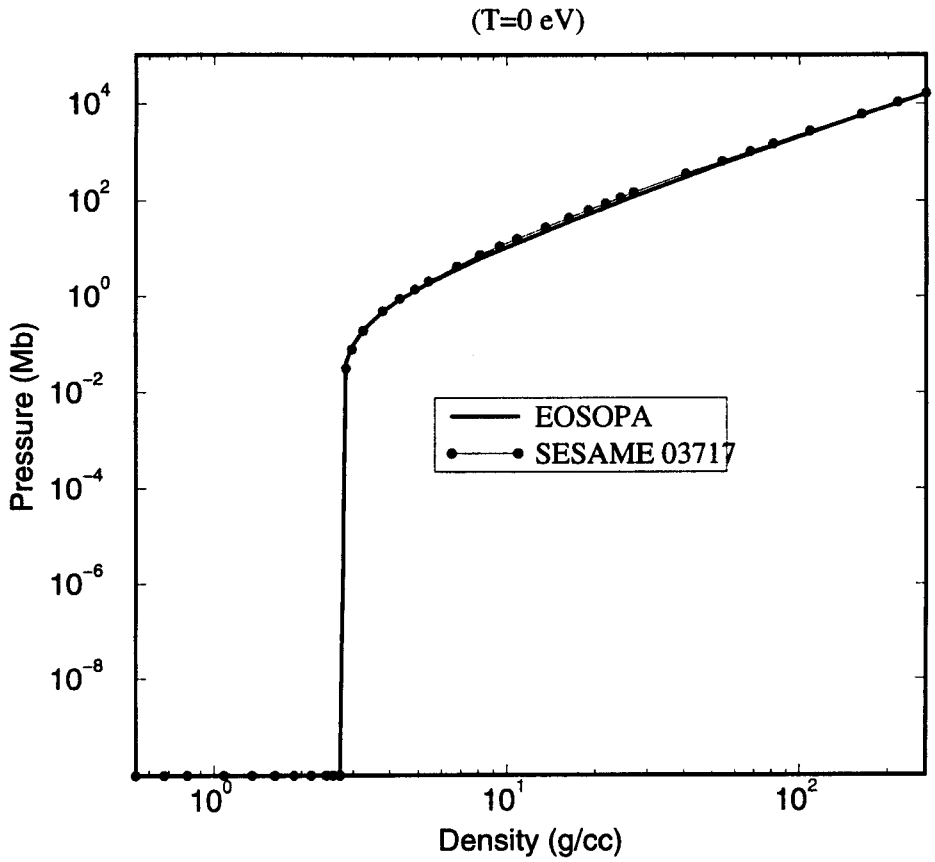

Figure 2.4. Comparison of Al zero temperature EOS calculated from EOSOPA and SESAME data. The SESAME data are taken from EOS Table 03717.

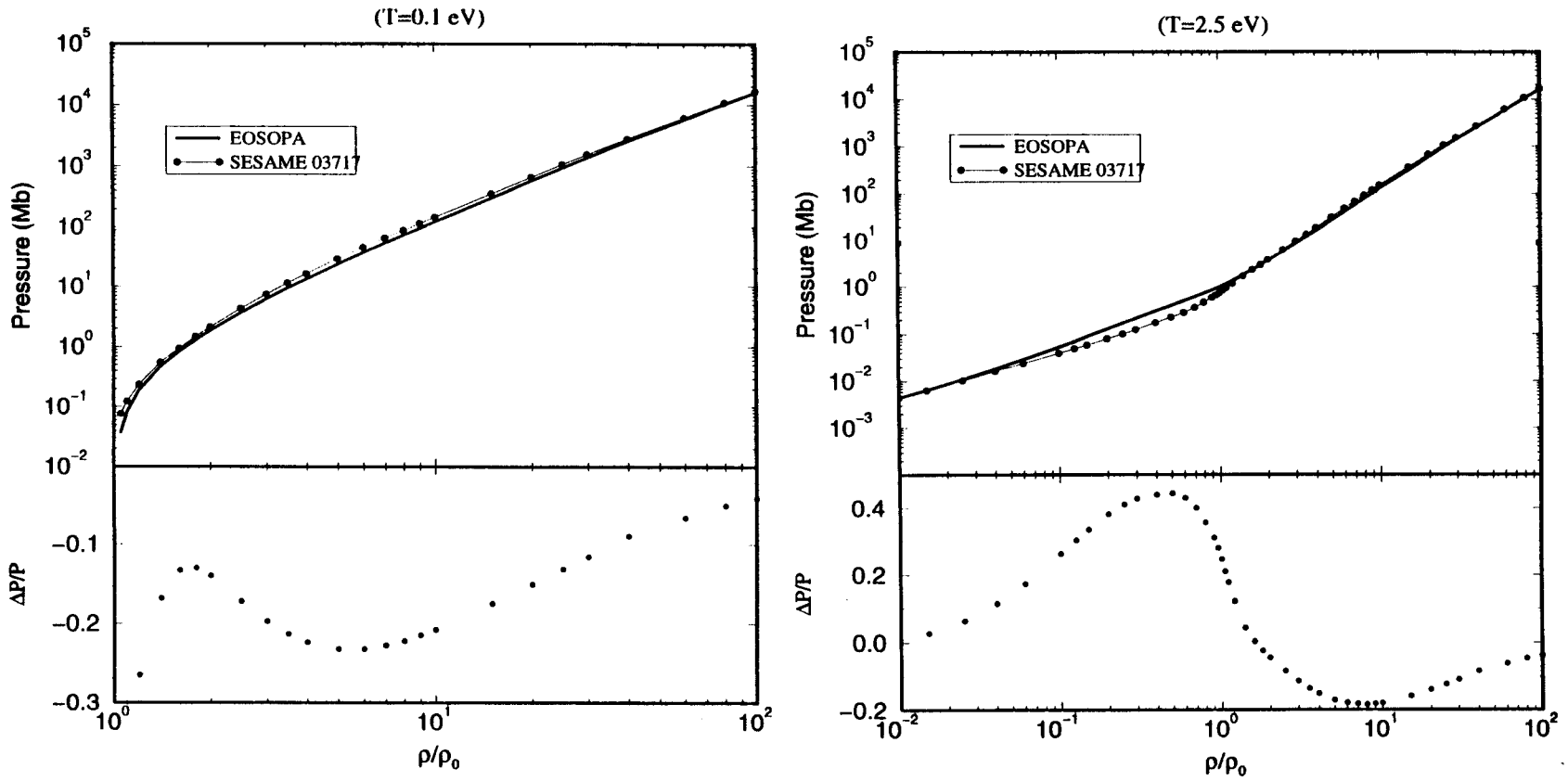

Figure 2.5. Comparison of low temperature aluminum pressure isotherms with the SESAME data. The SESAME data are taken from EOS Table 03717.

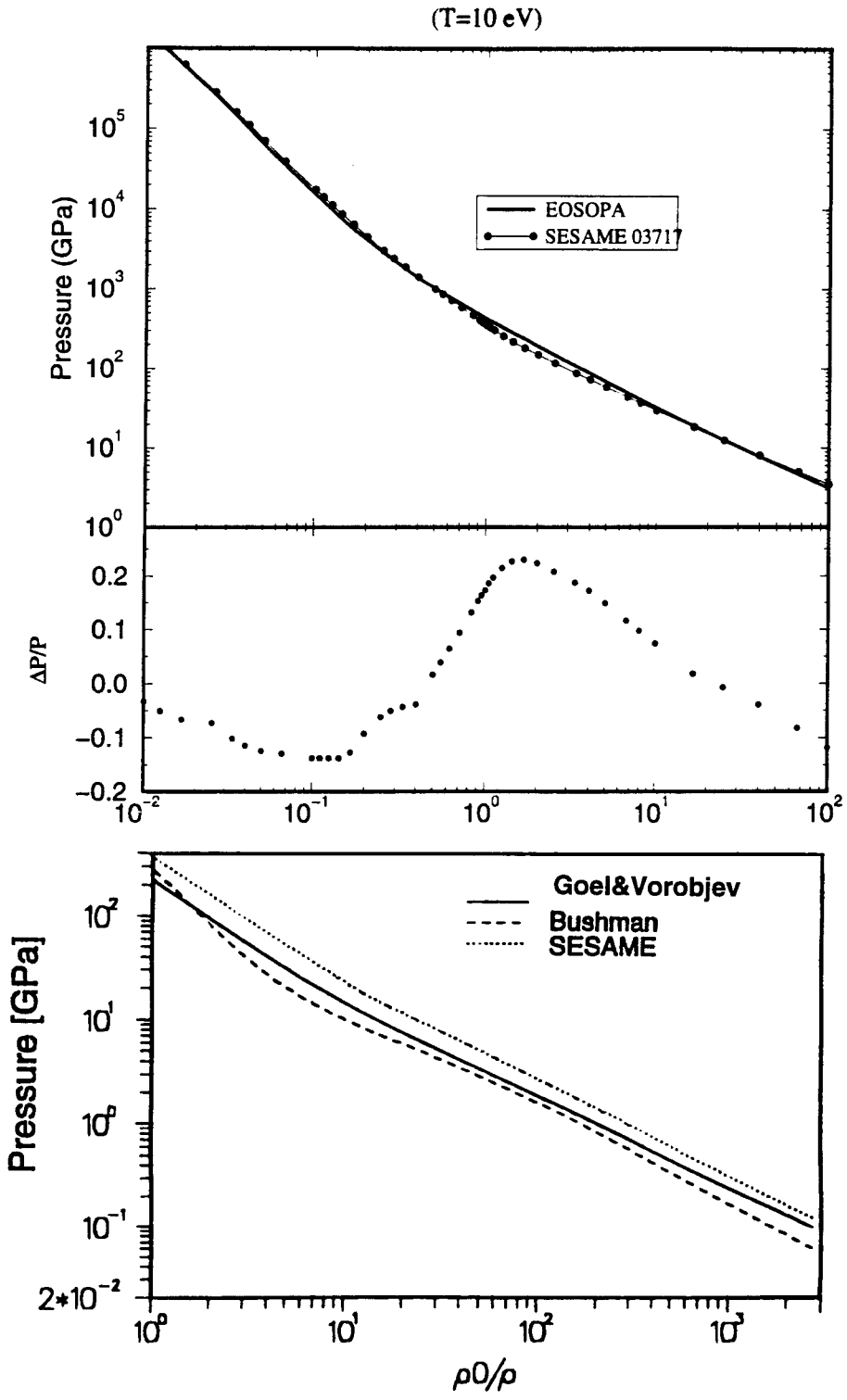

Figure 2.6. Aluminum pressure isotherm at $T = 10$ eV. Results of four different models are shown. Also shown are the relative errors between the data of EOSOPA and SESAME. The bottom plot is taken from Goel and Vorobjev [3], where $T = 9$ eV.

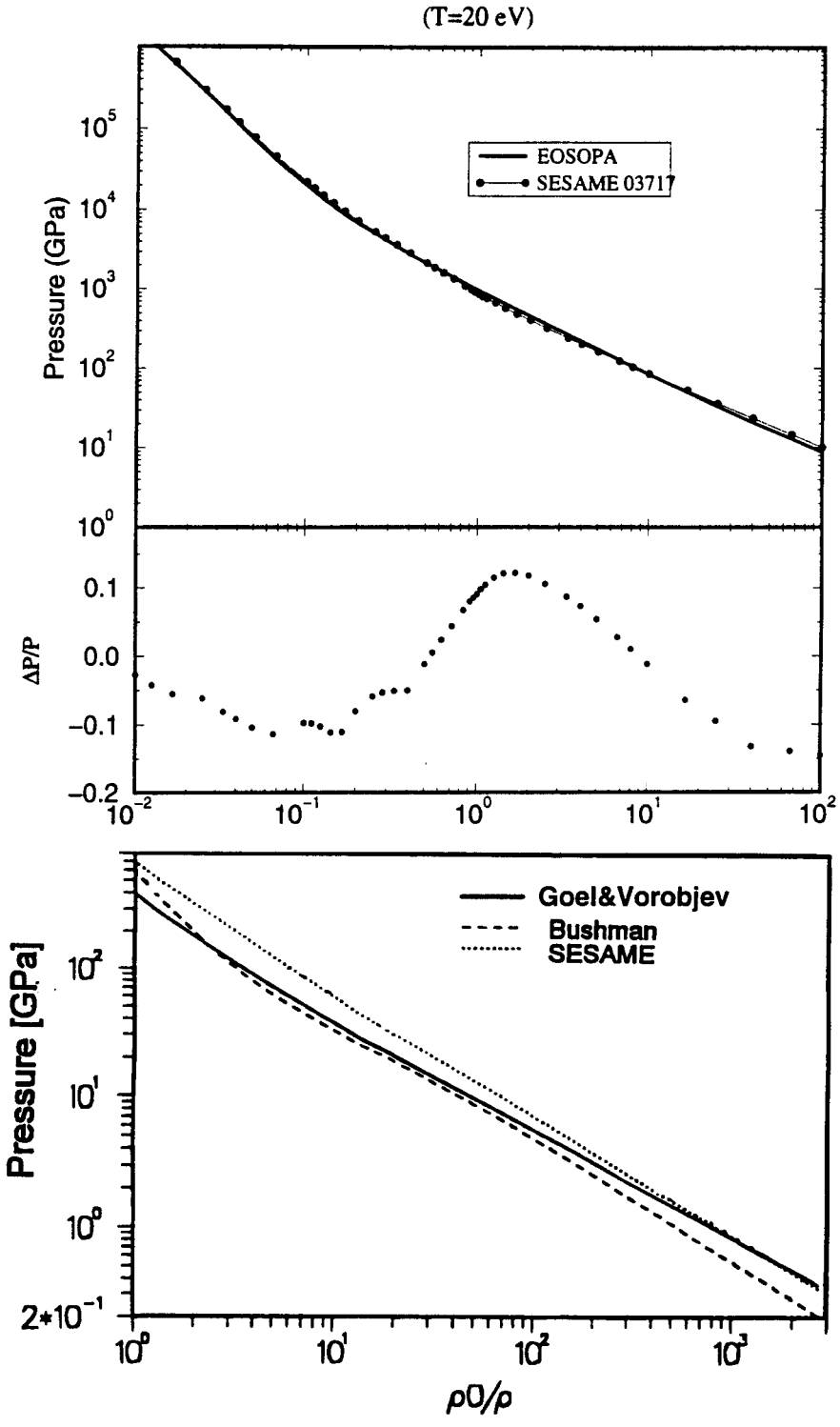

Figure 2.7. Aluminum pressure isotherm at $T = 20$ eV. Results of four different models are shown. Also shown are the relative errors between the data of EOSOPA and SESAME. The bottom plot is taken from Goel and Vorobjev [3], where $T = 17$ eV.

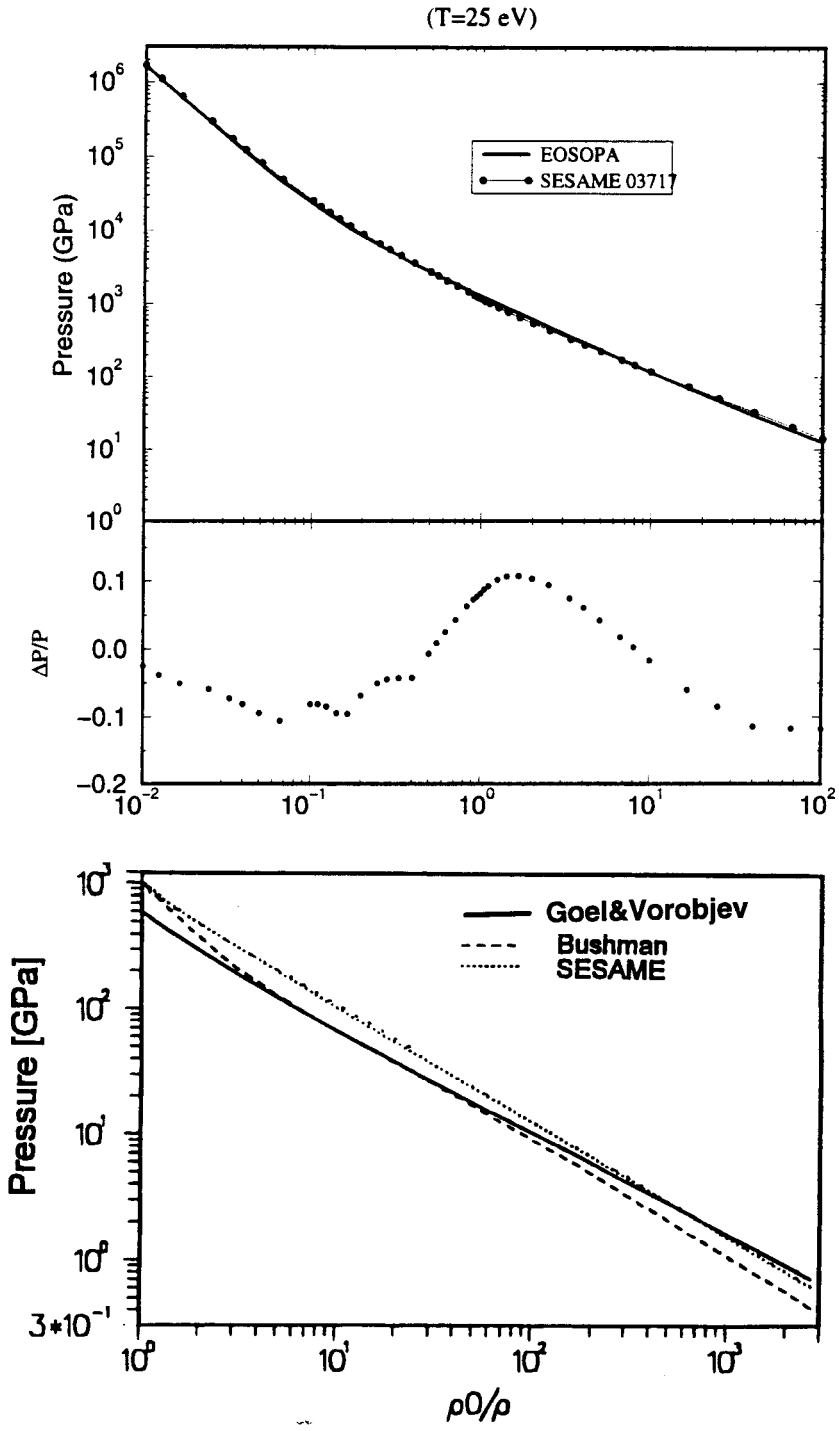

Figure 2.8. Aluminum pressure isotherm at $T = 25$ eV. Results of four different models are shown. Also shown are the relative errors between the data of EOSOPA and SESAME. The bottom plot is taken from Goel and Vorobjev [3], where $T = 25$ eV.

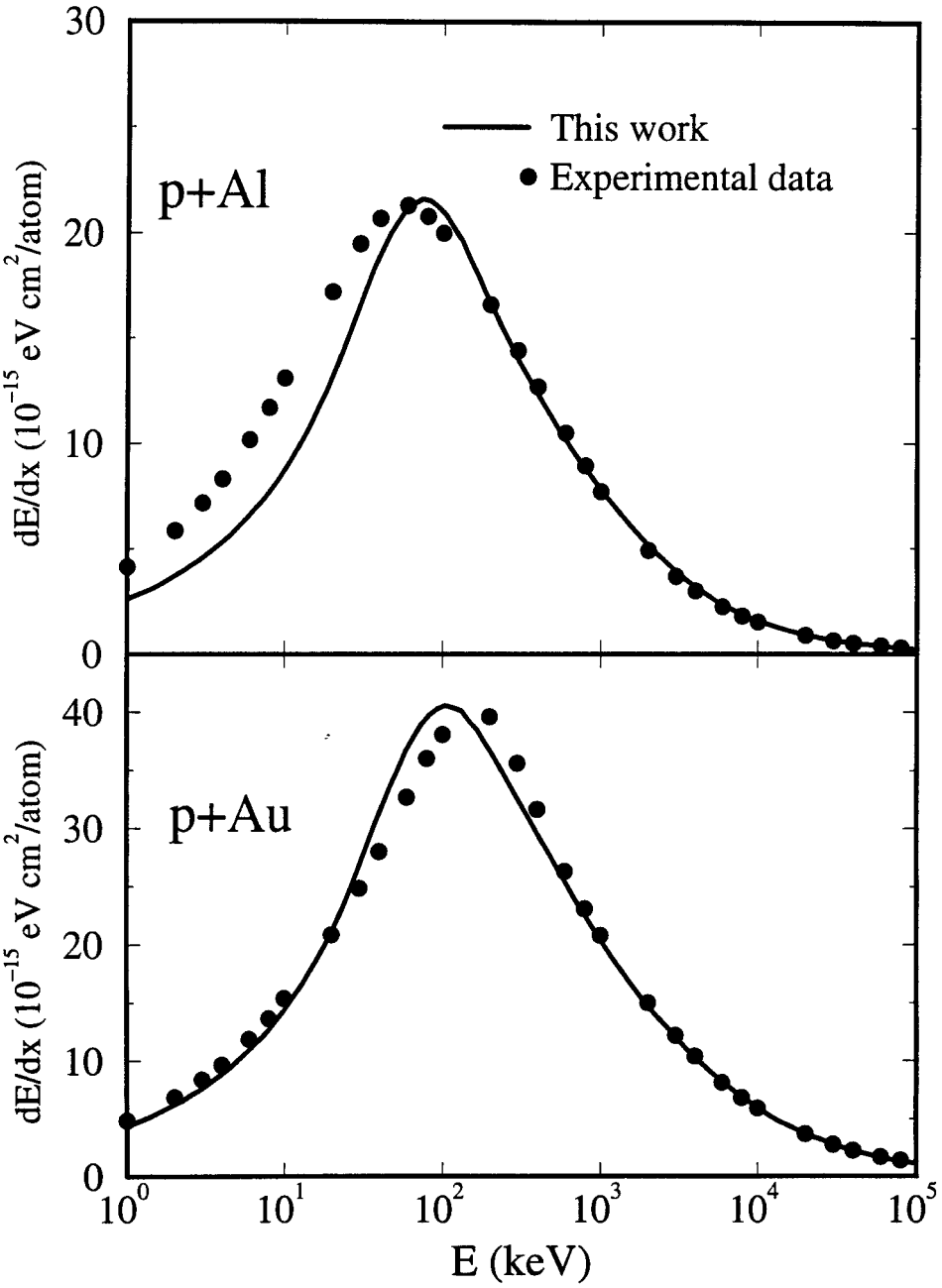

Figure 2.9. Proton stopping power in cold aluminum (upper) and gold (lower) targets. Results from our calculations are shown along with the experimental data.

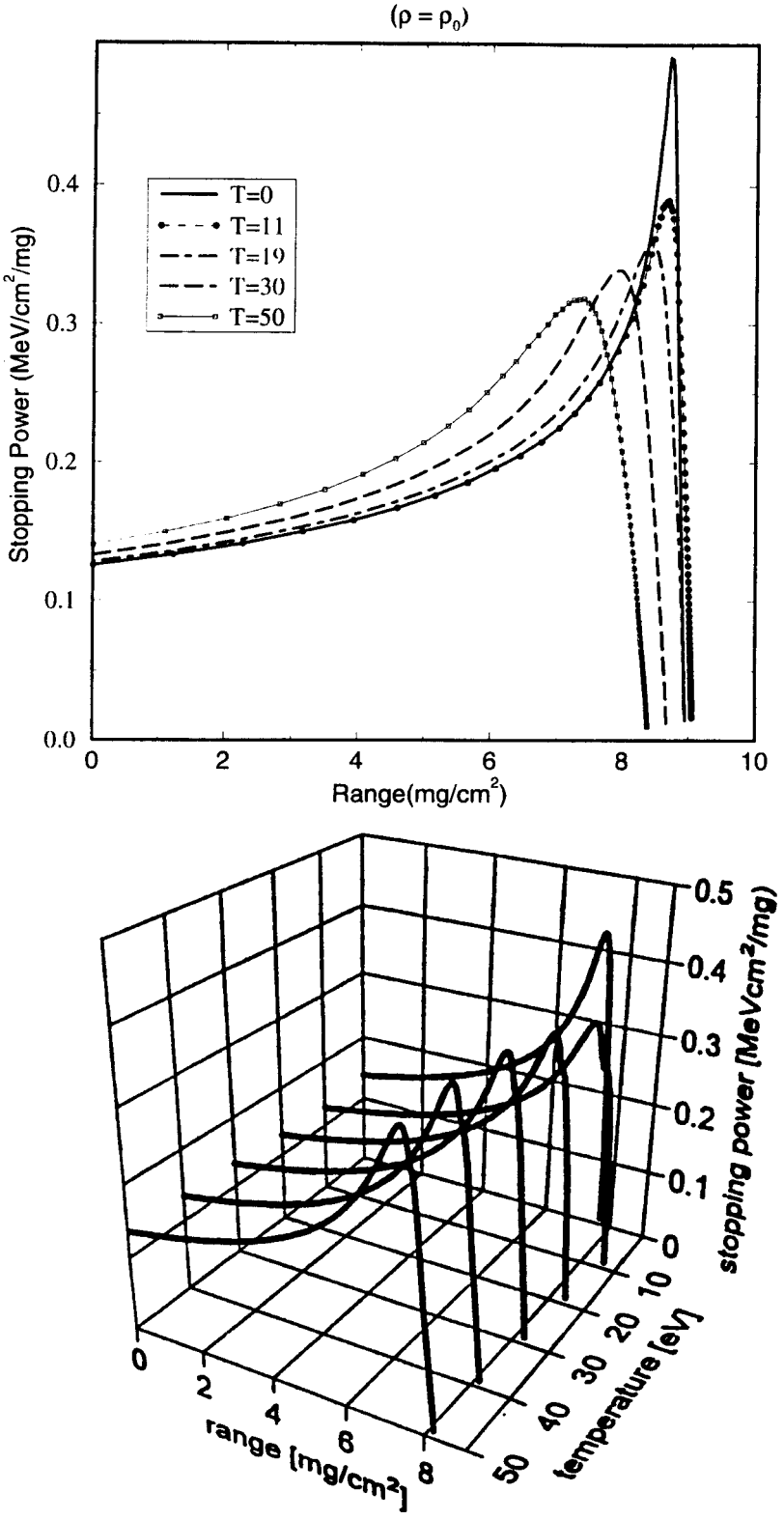

Figure 2.10. Dependence of stopping power for 1.7 MeV protons on penetration depth and temperature in an aluminum target with $\rho = 2.7$ g/cc. Results from our calculations (upper) are shown along with the results of Polyshchuk's semi-empirical model (lower).

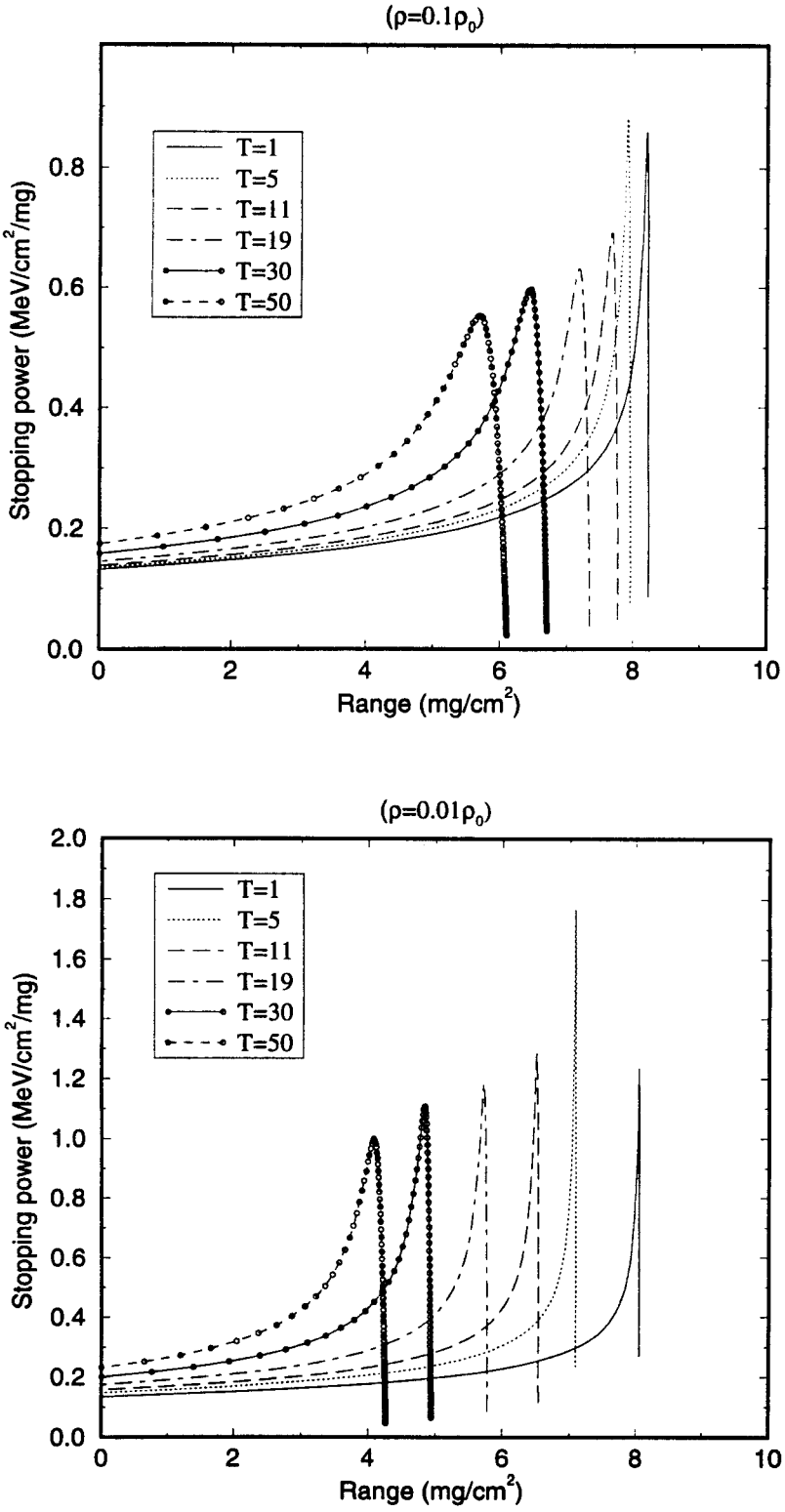

Figure 2.11. Dependence of stopping power for 1.7 MeV protons on penetration depth and temperature in an aluminum target with $\rho = 2.7$ g/cc and $\rho = 0.027$ g/cc. Results are calculated with the use of our unified SCF stopping power model.

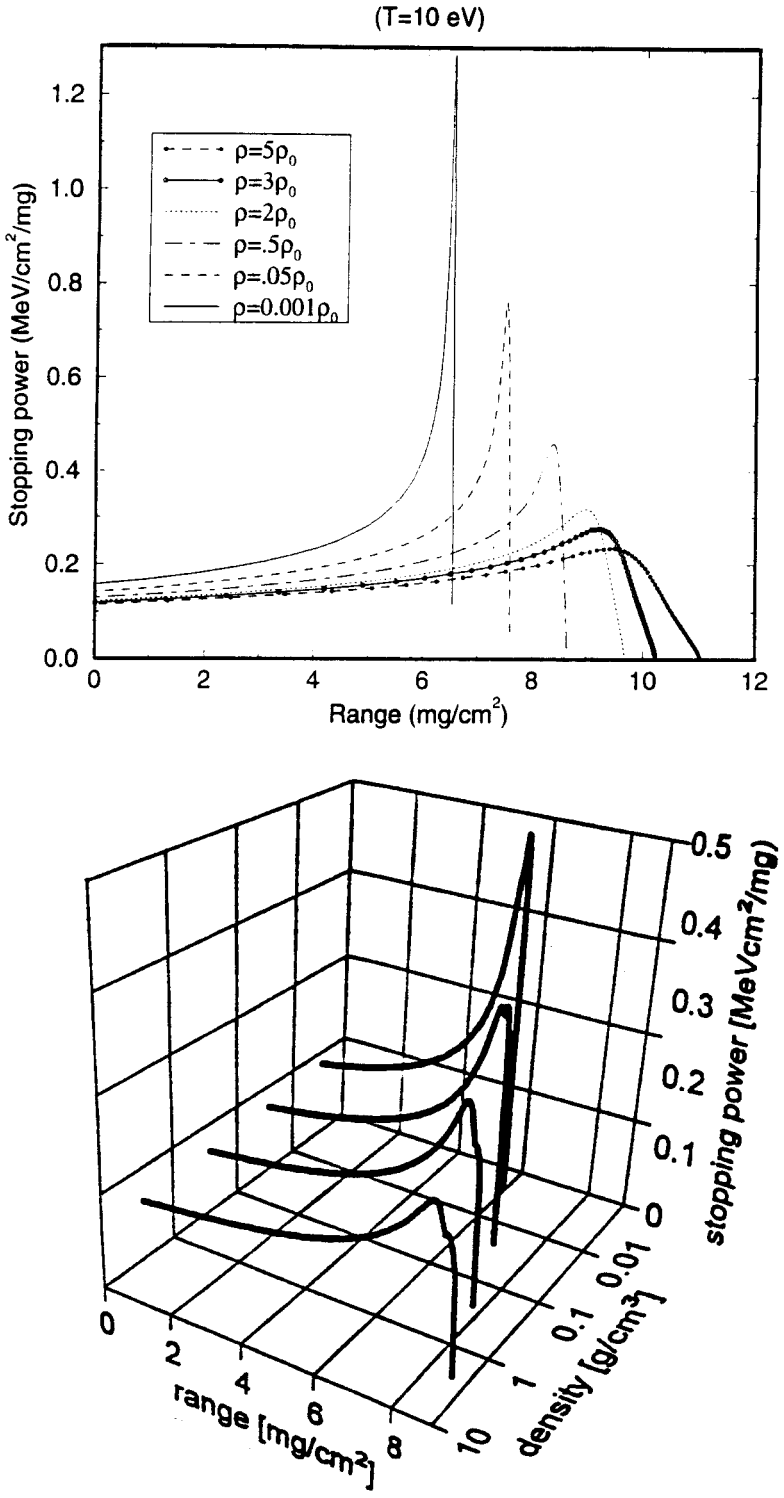

Figure 2.12. Dependence of stopping power for 1.7 MeV protons on penetration depth and density in an aluminum target with $T = 10$ eV. Results from our calculations (upper) are shown along with the results of Polyshchuk's semi-empirical model (lower).

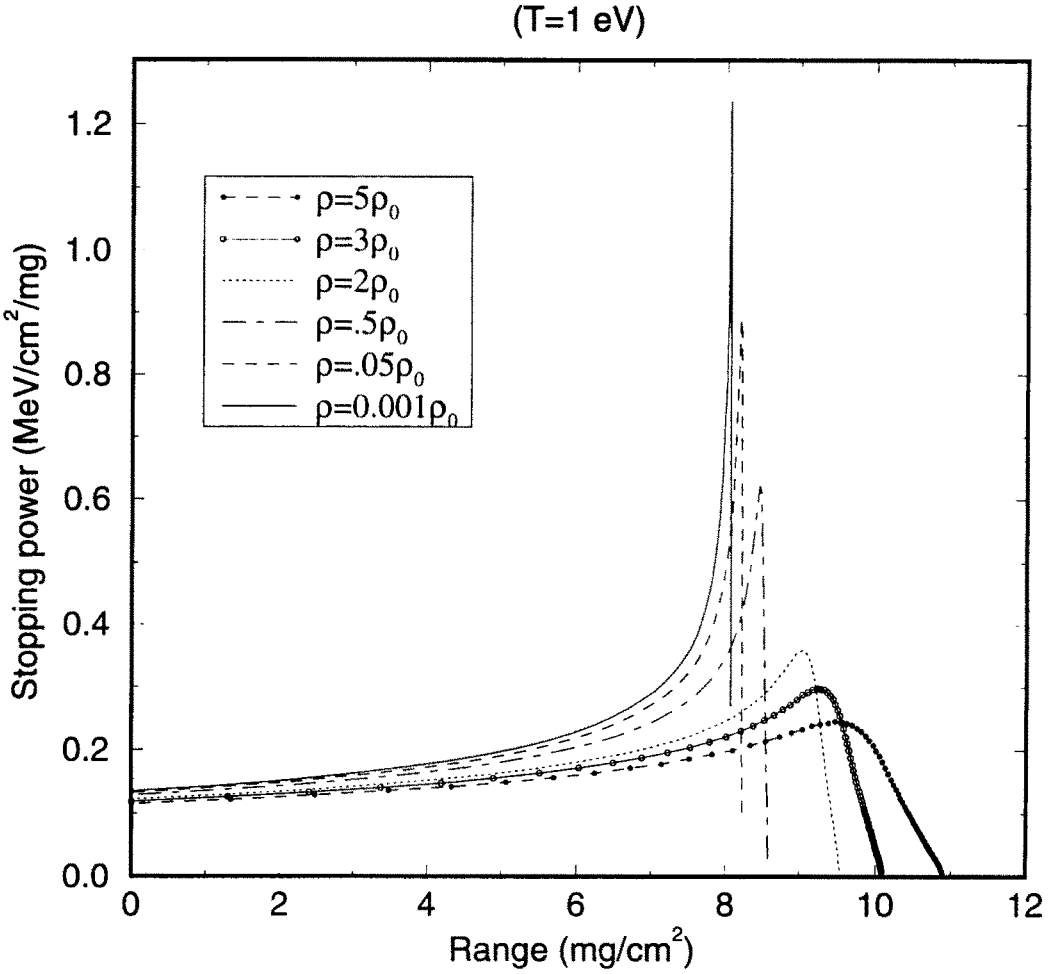

Figure 2.13. Dependence of stopping power for 1.7 MeV protons on penetration depth and density in an aluminum target with $T = 1$ eV. Results are calculated with the use of our unified SCF stopping power model.

Figures 2.10 through 2.13 show the variation in the stopping power of 1.7 MeV protons on aluminum targets in the temperature and density conditions relevant to the KALIF experiments. Also shown are the results calculated by the semi-empirical formulae developed by Polyshchuk et al. [15] and presented in Baumung [1]. It can be seen that there are some discrepancies between our results and those predicted with the semi-empirical model. First, our calculations tend to predict somewhat longer penetration depths. Since our calculated stopping powers for protons in cold aluminum agree very well with the experimental data, we believe that calculated results should provide better penetration depths. Secondly, the semi-empirical model predicts a fairly substantial increase in the range as the temperature increases from zero to 10 eV. Only a modest increase is seen in our result. At zero temperature and solid density, the range predicted from our model is 8.9 mg/cm^2, while that of the semi-empirical model appears to be about 7.8 mg/cm^2. The difference between our results and those of semi-empirical model is typically about 5 to 15 percent.

3. Radiation-Hydrodynamics Simulations

3.1. B_θ-Diode Simulations

Several simulations of B_θ-diode shock-wave experiments were performed in order to compare with previous work [3,4]. In the simulations, the proton beam was assumed to be monoenergetic with a time-dependent voltage and power density as shown in Figure 3.1. The voltage is initially about 1.3–1.4 MeV, and decreases after 40 ns. The peak power density is 0.15 TW/cm^2, while the peak current density is 0.17 MA/cm^2. It was assumed the protons travel along a trajectory perpendicular to the target. We note that if the incident proton beam hits the target at an angle substantially different from 90°, the depth at which the ions penetrate into the target will be reduced.

The calculations were performed using BUCKY-1 [16], a 1-D radiation-hydrodynamics code which includes ion energy deposition, radiation transport, and realistic equation of state and opacity data. Our baseline calculation is for a 50 μm-thick Al target with no LiF backing. Unless otherwise stated, we used a SESAME equation of state (Table 3717 [5]) and EOSOPA opacities. Generally, calculations were performed with no radiation transport. This was done because results with and without radiation transport were virtually identical (as discussed below). The stopping power model of Mehlhorn [17] was used for most simulations. Results obtained using the stopping power of Wang and Mehlhorn [13] for Al were found to be very similar.

Figure 3.2 shows results for the temperature, pressure, density, and fluid velocity as a function of mass (position) in the target at simulation times of 5, 10, 20, and 40 ns. The total thickness of the target is 13.5 mg/cm^2 (50 μm). Figure 3.3 shows the corresponding profiles for the time-integrated ion energy deposited in the target. The results show the ions deposit their energy in the first 5–6 mg/cm^2 of Al ($\Delta L = 14 - 16$ μm at solid density). The leads to two very distinct regions in the target: (1) the ion deposition region, which is characterized by relatively high temperatures and low densities; and (2) a shock propagation region, which remains relatively cold and dense. The pressure at the interface between these two regions is 0.2 Mbar at $t \lesssim 10$ ns, and falls somewhat at later times. This dropoff occurs despite the increase in the beam power density out to $t = 40$ ns. The increase in peak pressure near the Al rear surface ($m = 13.5$ mg/cm^2) at $t = 5$ ns shows the initial strong shock breaking through the back of the target.

Note that the fluid velocity can increase dramatically near the boundary of the rear surface. This is most clearly seen at $t = 10$ ns (solid curve). This occurs as the initial strong shock "reflects" off the rear surface. The observational significance of this high-velocity, decompressing blowoff is not clear at this time. If the laser light from the ORVIS diagnostic penetrates through this blowoff, it should see into the dense material which has a fairly flat velocity profile. Figure 3.4 shows the fluid velocity of various Lagrangian mass elements as a function of time. At 5 ns, the shock breaks out of the rear side, accelerating the outermost zones to relatively high velocities.

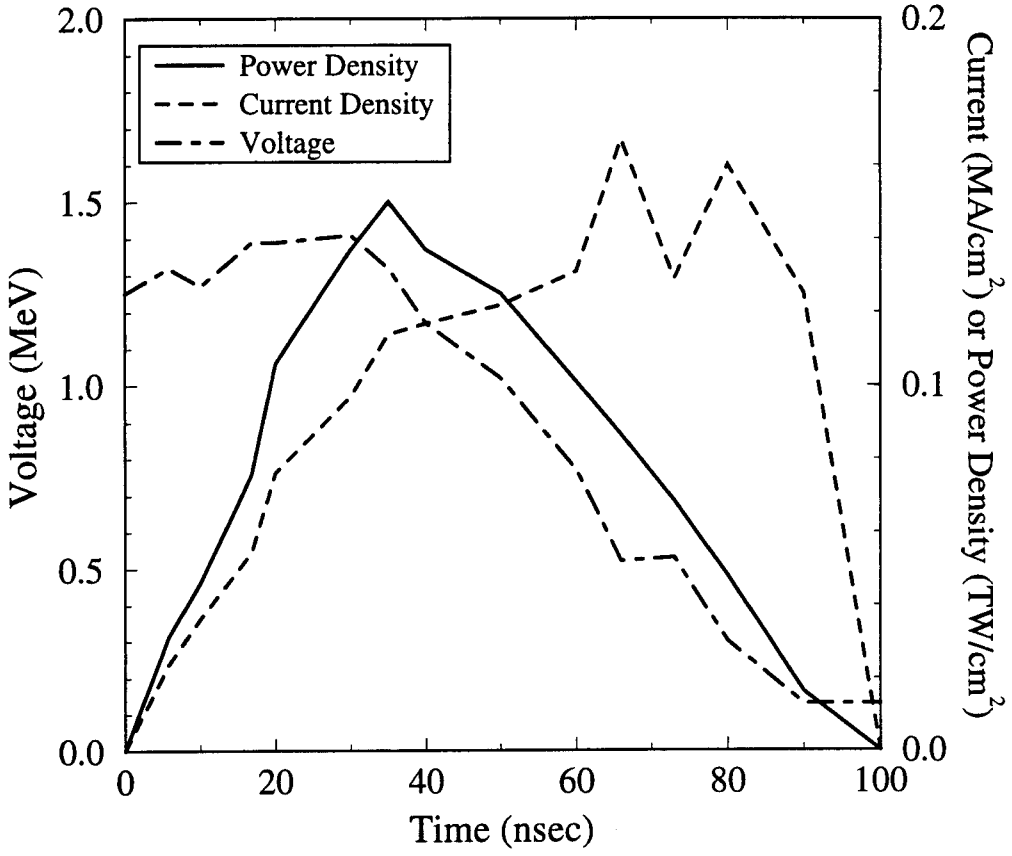

Figure 3.1. Time-dependent beam parameters used in simulation of KALIF B_θ-diode shock-wave experiments.

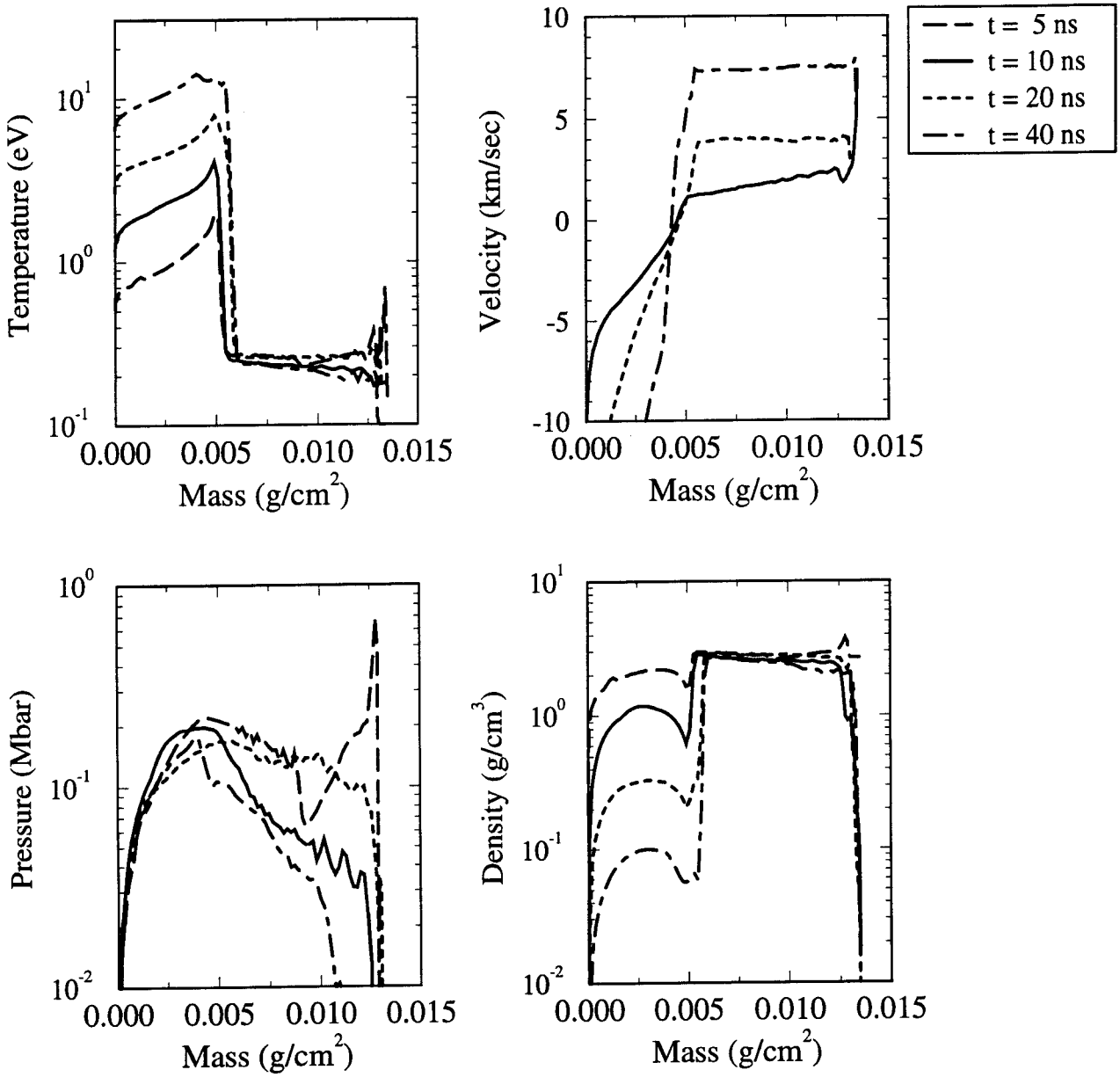

Figure 3.2. Spatial dependence of temperature, pressure, fluid velocity, and mass density at simulation times of 5, 10, 20, and 40 ns for the B_θ-diode shock-wave experiment. The beam enters the 50 μm-thick Al target at the left in each plot.

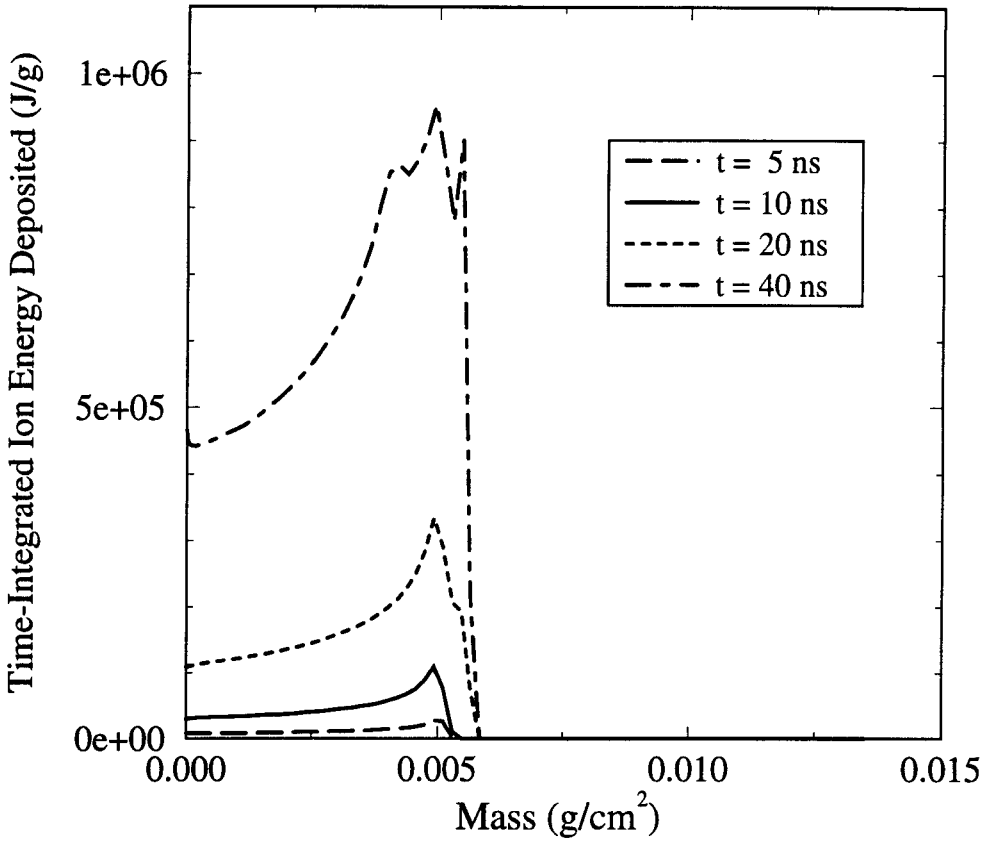

Figure 3.3. Spatial dependence of time-integrated ion energy deposition at simulation times of 5, 10, 20, and 40 ns from the 50 μm Al B_θ-diode simulation.

Their velocity stays nearly constant until a second, weak shock (resulting from reverberations) passes through. The deeper zones are seen to exhibit a smoother increase in velocity. Also, there is a weaker dependence of the velocity on position at points deeper in the target. In the analysis below, it will be assumed that the laser light of the ORVIS diagnostic penetrates through this high-velocity, low-density blowoff, and sees to a depth of ≈ 1 mg/cm^2 ($m = 12.5$ mg/cm^2 in Figure 3.4).

Figure 3.5 shows the energy partitioning in the target as a function of time. In this simulation radiation transport effects were included. Note that the total radiative energy lost is only a very small fraction of the total energy. Of the total energy deposited in the target, most of it is stored as internal energy in the plasma, while the remainder is converted to kinetic energy.

We next compare our results with those obtained in previous analyses of the B_θ-diode shock-wave experiments [3,4]. Figure 3.6 shows results for the rear surface velocity as a function of time. Here, it is arbitrarily assumed the rear surface velocity is given by the velocity of a fluid element located 1 mg/cm^2 from the outermost zone in the hydrodynamics simulation. The baseline case uses the SESAME EOS for Al and the Mehlhorn stopping power model, and is represented by the solid curve in Figure 3.6. For comparison, results from Goel and Vorobjev [3] are shown in the bottom plot. For convenience to the reader, results of the 50 μm-thick Al calculation of Goel and Vorobjev using the SESAME EOS have been added to the top plot with a time offset of $\Delta t = 5$ ns. Also shown as crosses in the bottom plot are experimental data points. Note that the $t = 0$ point for the abscissa in the top plot corresponds to the simulation time the proton beam starts to irradiate the target. In the bottom plot, $t = 0$ corresponds to the time the ORVIS diagnostic begins to record a moving surface. At $t \approx 5$ ns in our simulations, the initial shock breaks through the Al rear surface.

Although the results from the two simulations are qualitatively similar, there are some notable discrepancies. There are several possible causes of this discrepancy. First, there are several "SESAME" EOS tables for Al. Thus, although both simulations use SESAME data, there may still be differences in the EOS used. Second, the velocity curve from our BUCKY-1 simulation corresponds to a point at a depth of 1 mg/cm^3 from the rear surface. As noted above, there is some dependence of the fluid velocity on the depth. Thus, it seems important to know how deep the laser light from the ORVIS diagnostic penetrates before it is reflected. Third, the stopping power models in the two simulations are different. Since the reverberation time for shocks depends on the width of the shock propagation region, any differences in the computed ranges will lead to discrepancies in the results. And fourth, the offset between the time the beam starts to irradiate the target and the time the ORVIS diagnostic records the first shock breakout is evidently not accurately known. Thus, the assumed offset of 5 ns may not be accurate.

The sensitivity of the rear surface velocity to the stopping power and EOS models is shown in Figure 3.7. The upper plot compares results using the SESAME EOS data and EOSOPA [6]

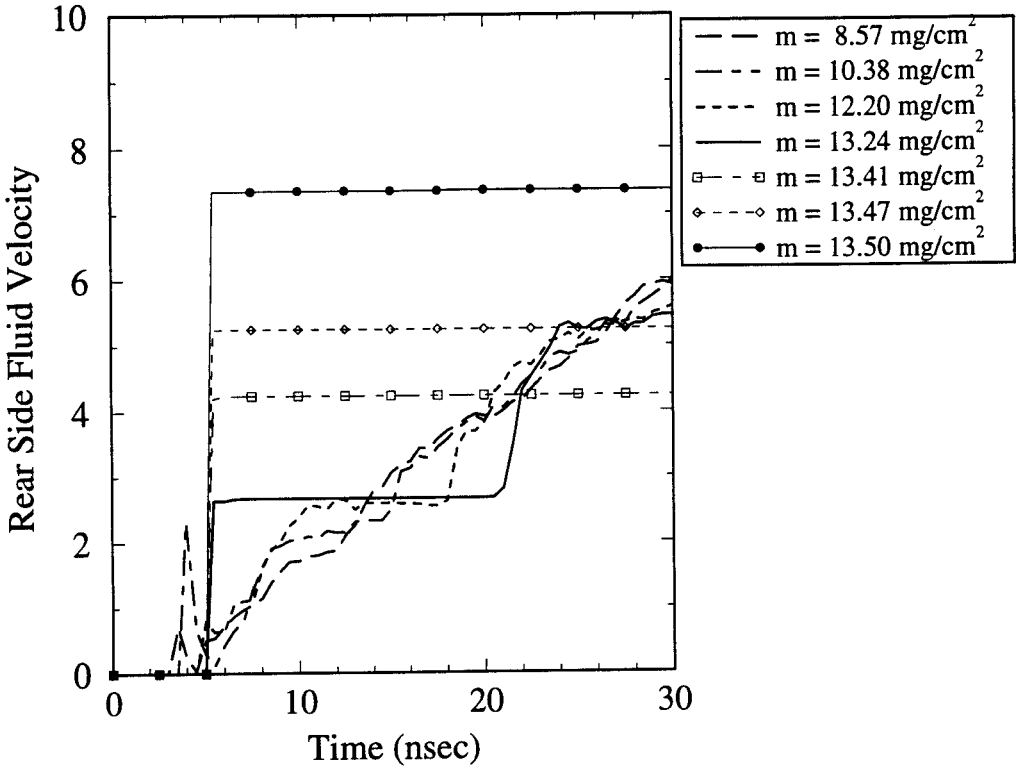

Figure 3.4. Time-dependent fluid velocity of mass elements in B_θ-diode simulation. The rear surface corresponds to $m = 13.50$ mg/cm^2.

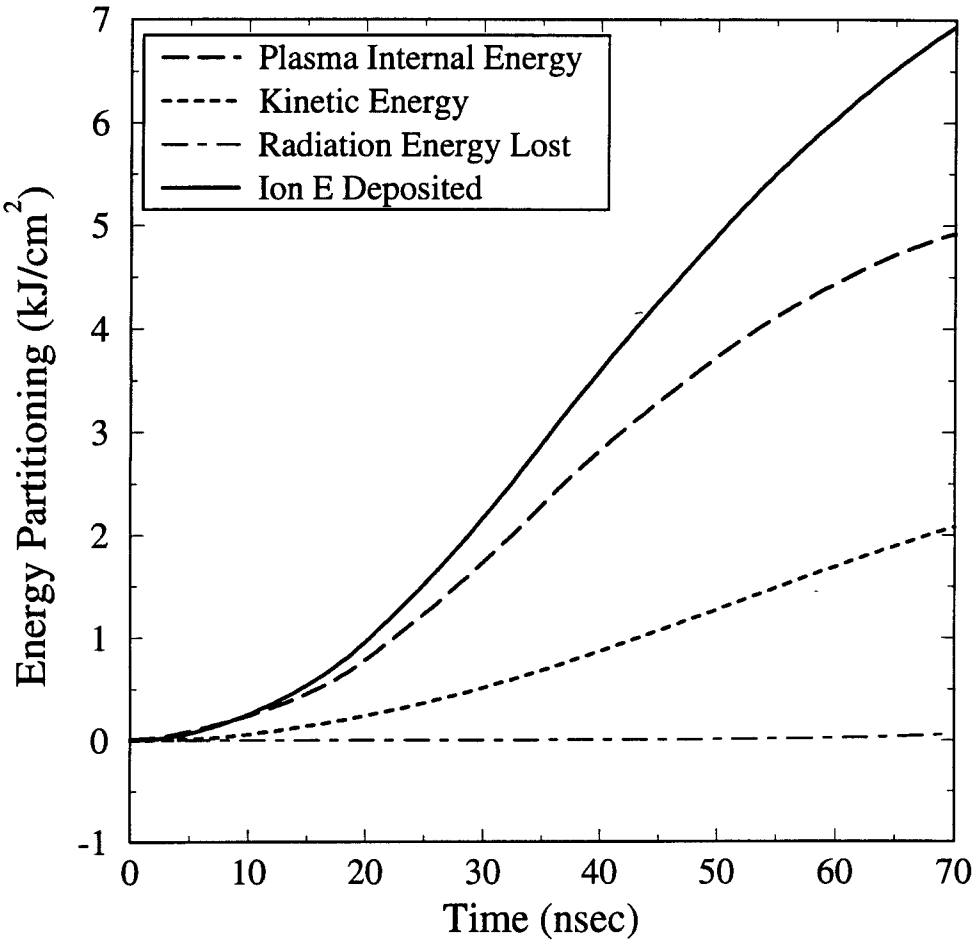

Figure 3.5. Time-dependence of energy partitioning in 50 μm Al B_θ-diode simulation.

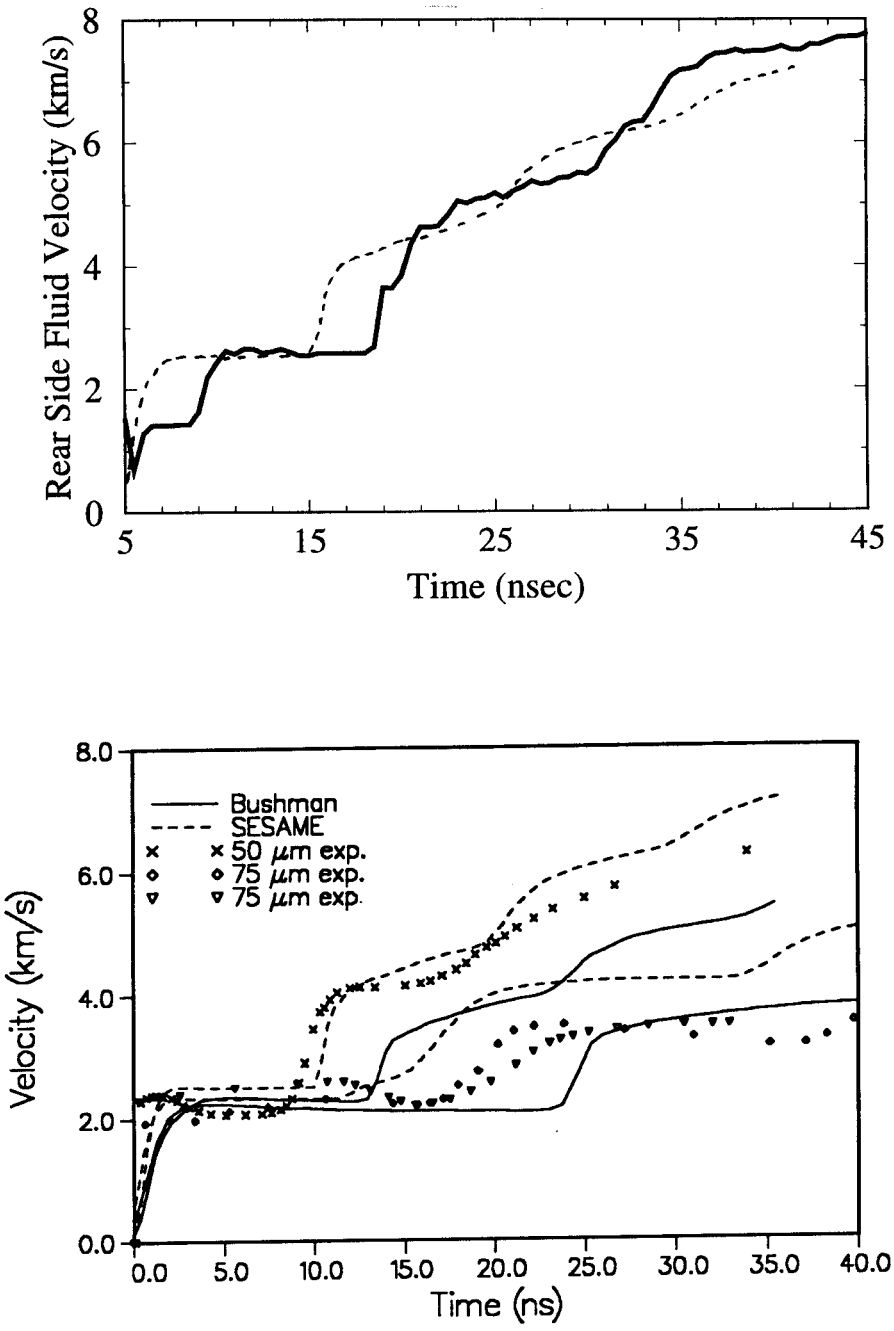

Figure 3.6. (Top) Rear surface velocities for B_θ-diode experiment with 50 μm-thick Al target calculated using BUCKY-1 (solid curve) and from Goel and Vorobjev [4] (dashed curve). (Bottom) Comparison of calculated and experimental B_θ-diode data from Goel and Vorobjev [4].

EOS data. The velocities at early times are higher when using the EOSOPA data. This occurs because EOSOPA predicts a higher pressure ($\sim$ tens of percent) than SESAME for a given energy in the ion deposition region of the target. At early times in the ion deposition region, $\rho/\rho_0 \sim 10^{-1} - 10^{0}$ and $T \sim$ a few eV.

The dependence of the rear surface velocity on the stopping power is shown in the bottom plot of Figure 3.8. The solid and long dashed curves represent results using the stopping power models of Mehlhorn [17] and Wang and Mehlhorn [13], respectively. Note that the velocity profiles are very similar. Calculations were also performed in which the Mehlhorn dE/dx was multiplied by factors of 0.8 and 1.2, which are shown as dotted and dash-dotted curves in Figure 3.7. When the stopping power is enhanced (dash-dotted curve) the range shortens, which leads to a thinner ion deposition and thicker shock propagation region. This leads to the longer shock reverberation times seen in the figure. It is also worth noting that the results with the dE/dx multiplier of 1.2 would be very close to the Goel and Vorobjev results if the offset in time was adjusted by an additional 4–5 ns. This would be consistent with the shorter range predicted by their semi-empirical model, as discussed in Section 2.2.

The above results seem to indicate that the uncertainty in the EOS probably leads to a somewhat greater potential source of error in analyzing the experimental data than the stopping power model. This simply results from the fact that the stopping power models are thought to be accurate to $\lesssim 20\%$, while the calculated EOS data in the temperature and density of the ion stopping region are probably susceptible to much greater uncertainty. Also, the above results were all obtained using the same proton beam parameters. The sensitivity of results to the beam parameters is discussed in the next section.

Finally, Figure 3.8 shows the results for a series of targets using the B_θ diode beam. The target thicknesses are 33, 50, and 75 μm. The bottom curve corresponds to a 33 μm-thick Al target backed by 1 mm of LiF. The BUCKY-1 results (top plot) are seen to be in rough qualitative agreement with the results of Goel and Vorobjev [4] and the experimental data (bottom plot).

3.2. Applied-B Diode Simulations

We next discusss results from simulations of KALIF shock-wave experiments in which the applied-B diode was used. In this analysis, a somewhat different approach was taken in comparing the experimental rear surface velocity with simulation. Here, the EOS and stopping power models were held fixed, but the time-dependent beam voltage and current density were adjusted until agreement with experimental velocity data was achieved. Results are then compared with those obtained using the experimentally diagnosed beam data. In addition, the sensitivity of the velocity profiles to assumed beam parameters and target EOS are discussed.

Figure 3.9 shows results for the cases of 50 μm-thick Al with no LiF backing and the 33 μm-thick Al with LiF backing. The squares represent applied-B diode experimental data, while the

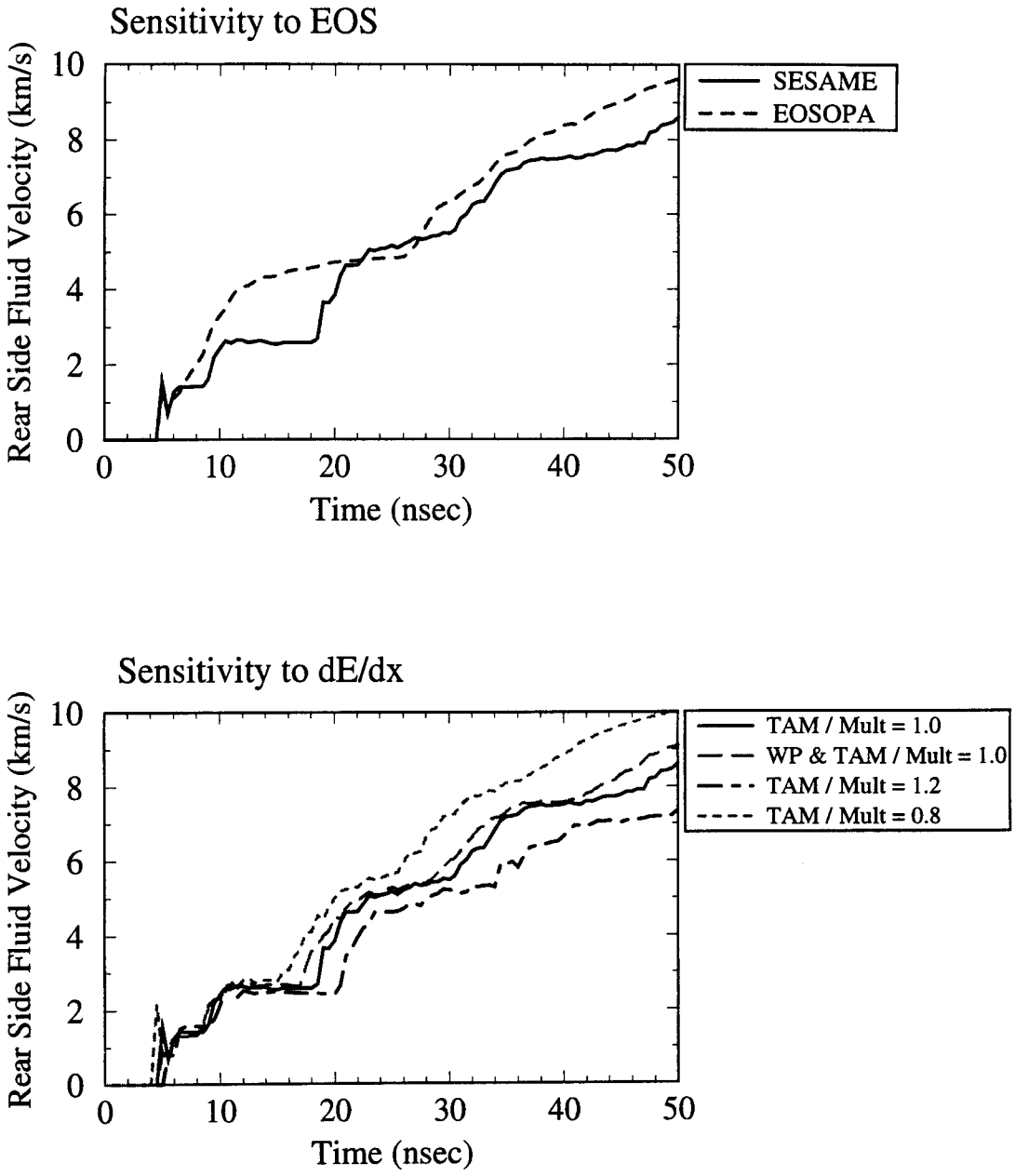

Figure 3.7. (Top) Comparison of rear surface velocities for B_θ-diode simulation using EOSOPA and SESAME data. (Bottom) Sensitivity of rear surface velocity to stopping power model. Results using Mehlhorn [17] model with various dE/dx multipliers are indicated by TAM; Wang and Mehlhorn [13] results are represented by the long dashed curve.

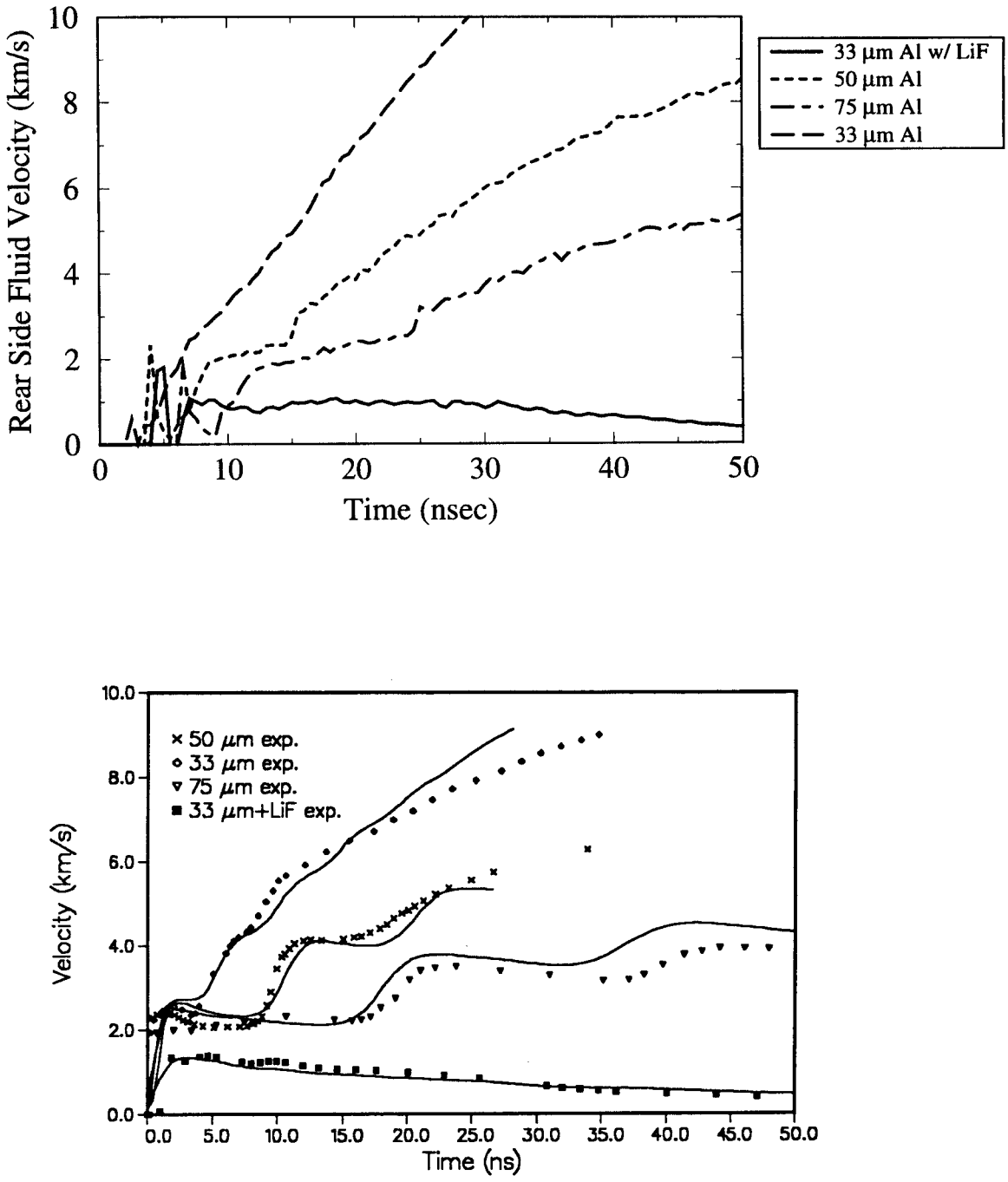

Figure 3.8. (Top) Time-dependence of rear surface velocities calculated for several B_θ-diode shock-wave experiments. (Bottom) Experimental and calculated results from Goel and Vorobjev [4].

solid curve represents the calculated fluid velocity at a depth of 1 mg/cm^3 from the rear surface. The experimental velocity data were offset in time to be consistent with the calculated breakout time of the initial shock. The good agreement was achieved by adjusting the time-dependent voltage and current density. The "fitted" beam parameters for this case are shown in Figures 3.10 and 3.11 (dashed lines with squares). In each case, the corresponding voltage and current density profiles deduced from experimental beam diagnostics are also shown (solid curves). The experimental curves were offset in time such that the current begins to rise from $t = 0$. The voltage histories used the same time offset. For the 50 μm case, the initial current rise during the first 15 ns is similar for the fitted and experimental values. Also a peak current density of 0.13 MA/cm^2 is predicted for both curves. For the 50 μm Al case, the voltage history (top plot) determined from the experimental diagnostics shows a pronounced drop in voltage from 1.1 MeV to 0.6 MeV at $t \approx 10$ ns, and then rises to a peak of 1.6 MeV before decreasing again at late times. Our fitted beam voltage exhibits an increase from 1.0 MeV to 1.7 MeV at $t = 20$ ns, followed by a drop in voltage after 25 ns. (It is interesting to note that adjusting the time offset of the experimental curve by $\sim 20 - 30$ ns would produce a much better qualitative agreement with the fitted voltage curve.)

The fitted and experimental voltage histories for the 33 μm case are in good agreement at $t \lesssim 10$ ns. At later times, the fitted voltage lies below the experimental curve. The fitted current density is found to be substantially lower than that deduced from the experimental diagnostics. It is important to note, however, that the fitted beam parameters do not represent a *unique* solution to the experimental rear surface velocity measurements.

Hydrodynamics simulations were also performed for the two target cases using the experimentally-deduced beam histories. These results are shown in Figure 3.12 along with the "fitted" results. In the 33 μm case (bottom plot) the rear surface velocity at $t \lesssim 20$ ns and $t \gtrsim 40$ ns is substantially higher than the measured velocities. This results from using a substantially higher current density than for the fitted case (see Figure 3.11). In the 50 μm case, a much longer reverberation time is exhibited (out to $t \approx 25$ ns). This results from the lower voltage at $t = 5 - 20$ ns. The lower voltages lead to a thinner ion deposition region, and therefore thicker shock propagation region.

Figure 3.13 shows for the 50 μm-thick Al case the spatial dependence of the temperature, pressure, density, and time-integrated ion energy deposited. Curves are shown for simulation times of 5, 10, 20, and 40 ns. The peak temperatures are seen to be $T \sim 10 - 20$ eV. These are similar to those in the B_θ diode simulation, which can be expected because of the similar current densities in the two simulations. At late times, the range of the protons drops (see upper right plot) due to a combination of two effects: a decreasing beam voltage and range shortening (hot stopping).

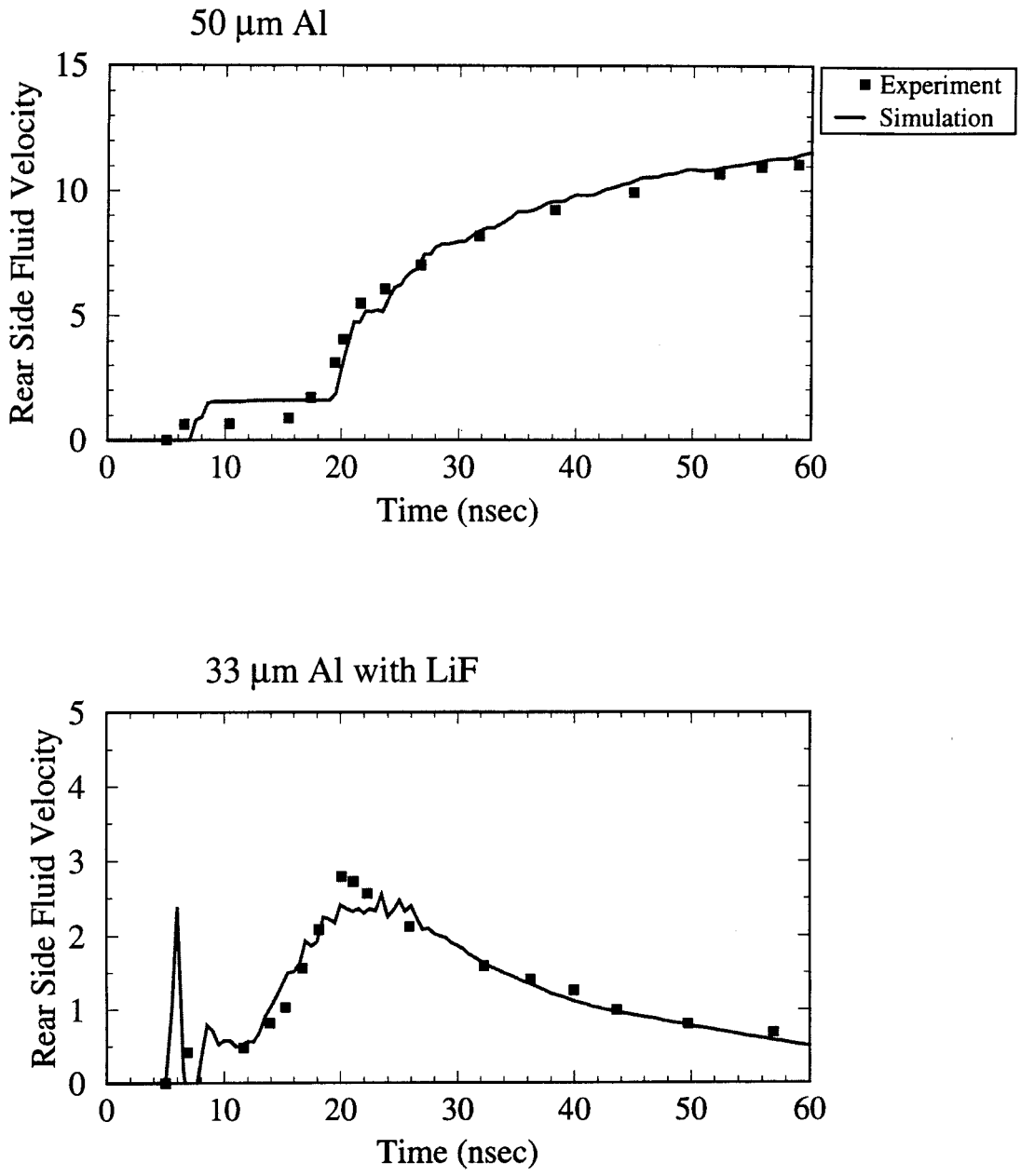

Figure 3.9. Comparison of calculated (solid curves) and experimental (squares) rear surface velocities for the KALIF applied-B diode shock-wave experiments. The beam parameters used in the simulations are shown in Figures 3.10 and 3.11.

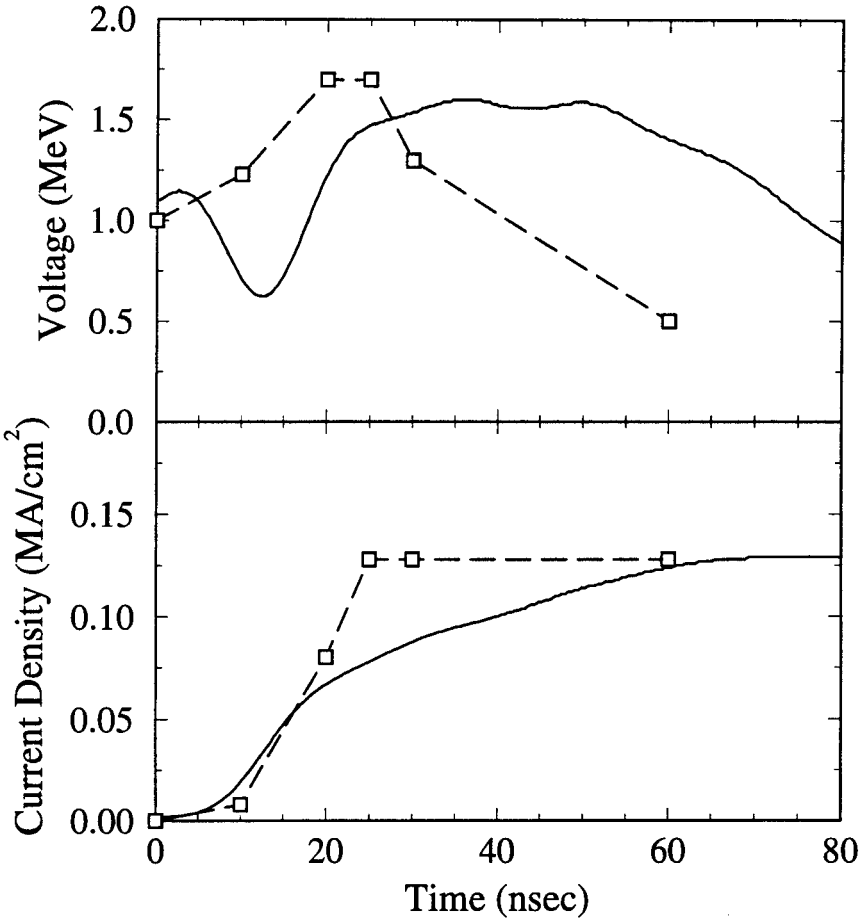

Figure 3.10. Dashed curves: beam voltage and current density profiles used in simulation of 50 μm-thick Al target irradiated by KALIF applied-B diode beam. Solid curves: beam parameters deduced from proton beam diagnostics.

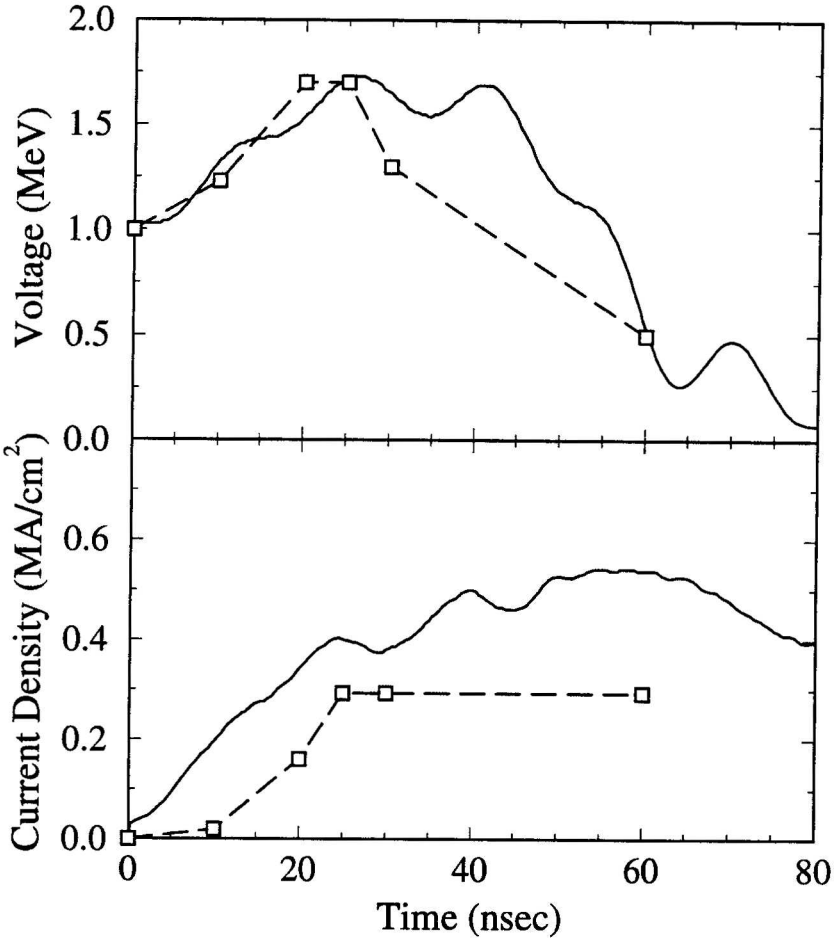

Figure 3.11. Same as Figure 3.10, but for 33 μm-thick Al target backed by LiF.

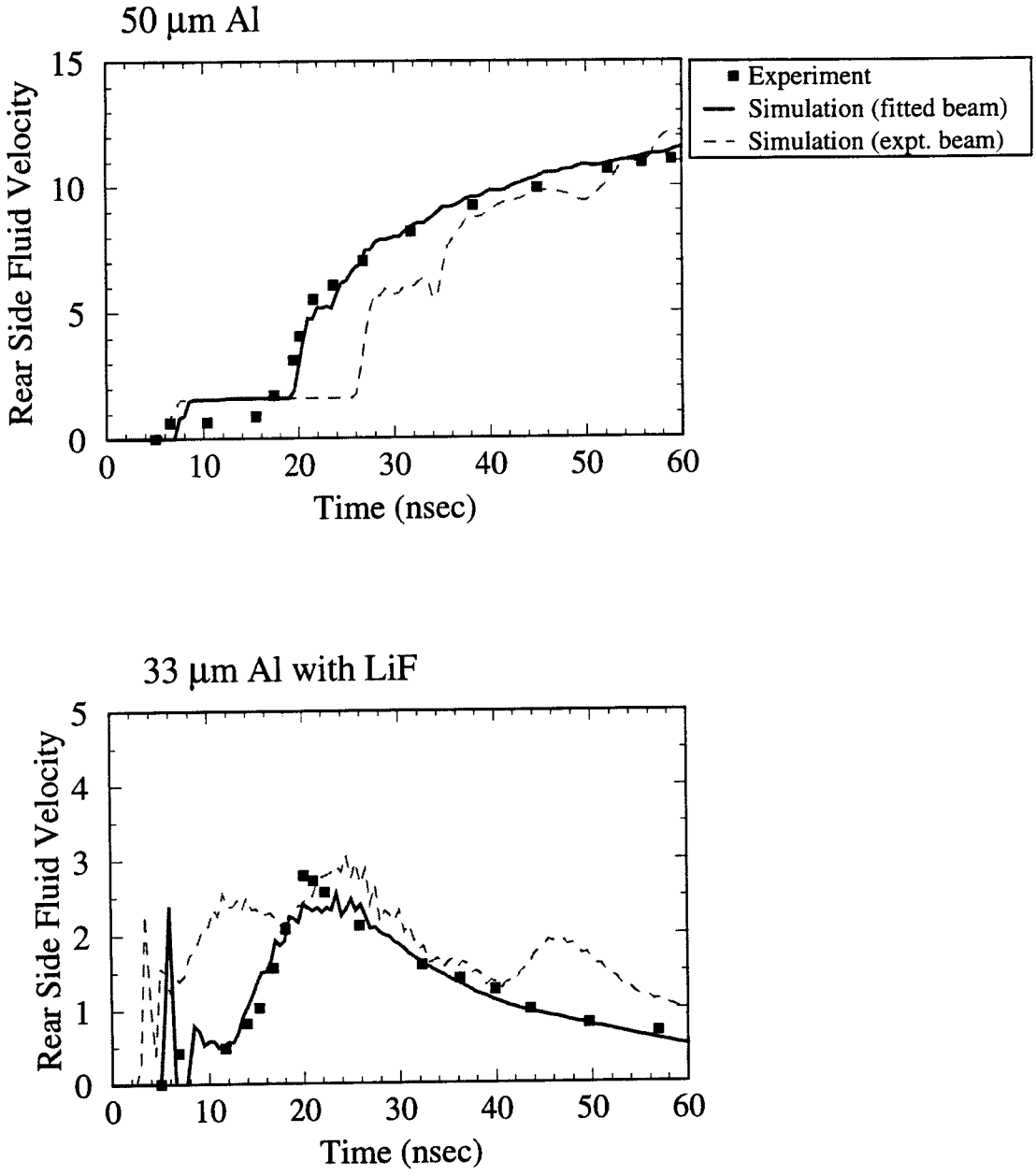

Figure 3.12. Comparison of rear surface results for "fitted" beam parameters (solid curves) and those deduced from the ion beam diagnostics (dashed curves). Experimental velocity data are represented by the squares.

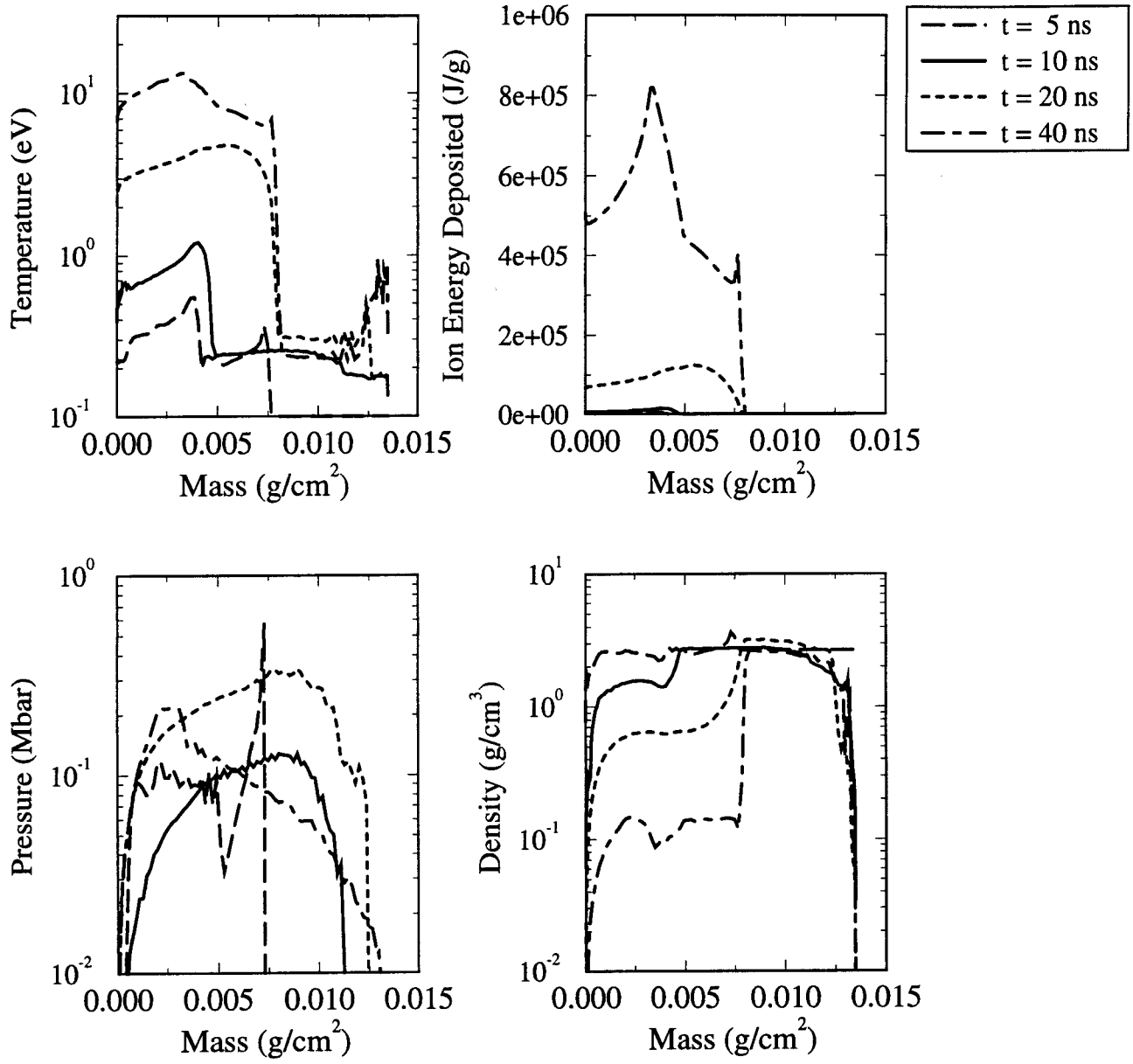

Figure 3.13. Spatial dependence of temperature, pressure, ion energy deposition, and density calculated at times of 5, 10, 20, and 40 ns in applied-B diode simulations of 50 μm-thick Al target.

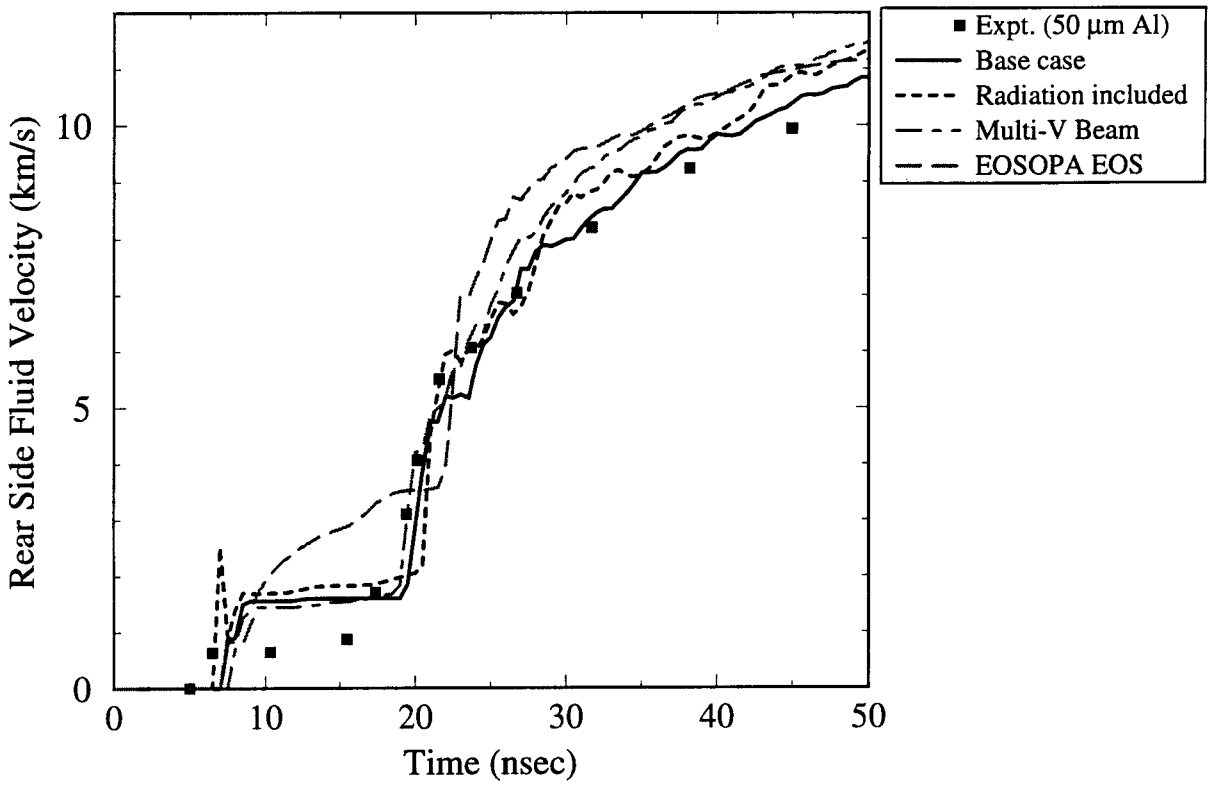

Figure 3.14. Sensitivity of calculated rear surface velocity to: radiation losses, a voltage spread in the proton beam, and equation of state.

The above results show that the experimental rear surface velocity data in the KALIF applied-B diode experiments can be reproduced in simulations where the beam parameters are adjusted within some "reasonable" range. We next examine in more detail the sensitivity of the results to the beam and target parameters.

For the 50 μm Al case, the influence of several physical variables on the resultant rear surface velocity was investigated. Figure 3.14 shows the rear surface velocity for several cases. The solid curve represents the "base" case, which neglects radiation losses, assumes a monoenergetic beam, and utilizes the SESAME EOS for Al. The dashed curve represents a simulation in which radiation effects were included. Clearly, radiation plays little role for these conditions. We also performed a simulation using a non-monoenergetic beam. Here, the beam was divided into 5 components with 10%, 20%, 40%, 20%, and 10% of the current being carried at voltages of $V = 0.8\,V_0$, $0.9\,V_0$, $1.0\,V_0$, $1.1\,V_0$, and $1.2\,V_0$, where V_0 is the time-dependent voltage. Note that the mean voltage, V_0, and total current density are identical to those in the base case. Using this multicomponent beam, the rear-surface velocity was found to be similar to the base case, but with somewhat higher velocities at late times (see dash-dotted curve).

The dashed curve in Figure 3.14 represents results using the EOSOPA EOS for Al. In this case, the differences with respect to the base case are more pronounced, particularly at early times. The rear surface velocity in the EOSOPA simulation is several tens of percent higher between 10 ns and 20 ns. This is due to the fact that EOSOPA predicts pressures $\sim$ tens of percent higher than SESAME for plasma conditions in the ion deposition region (see Section 2). At $t \lesssim 20$ ns, the plasma temperature is $\lesssim 3$ eV and the density is $\sim 0.2 - 1.0\,\rho_0$ in this region.

The effects of varying the time-dependent voltage or current density on the rear surface velocity, are shown for four cases in Figure 3.15. The base case is represented by the thick solid line. The dash-dotted curve with squares represents results from a simulation in which the current density was lowered in the $t \sim 20-50$ ns time frame to produce a more gradual increase in current (as is exhibited in the experimental curve in Figure 3.10). When this was done the rear surface velocity dropped below the experimental velocities at time $\gtrsim 20$ ns. The effect of maintaining a high voltage at late times is shown by the dashed curve with circles. In this case the current density was the same as in the base case, but the voltage was kept at 1.7 MeV at all times after 20 ns. The rear surface velocity at late times in this simulation is much higher than the measured velocities. This occurs because with a higher voltage the ions are able to penetrate deeper into the ion deposition region and continue to generate a higher pressure at the interface with the shock propagation region. Finally, the effect of lowering the early-time voltage is displayed by the dashed curve with triangles. This had only a minor effect on the velocity profile, as it mainly caused a slight delay in the time at which the original shock breaks out of the Al target.

A discussion and summary of these results is presented in Section 4.

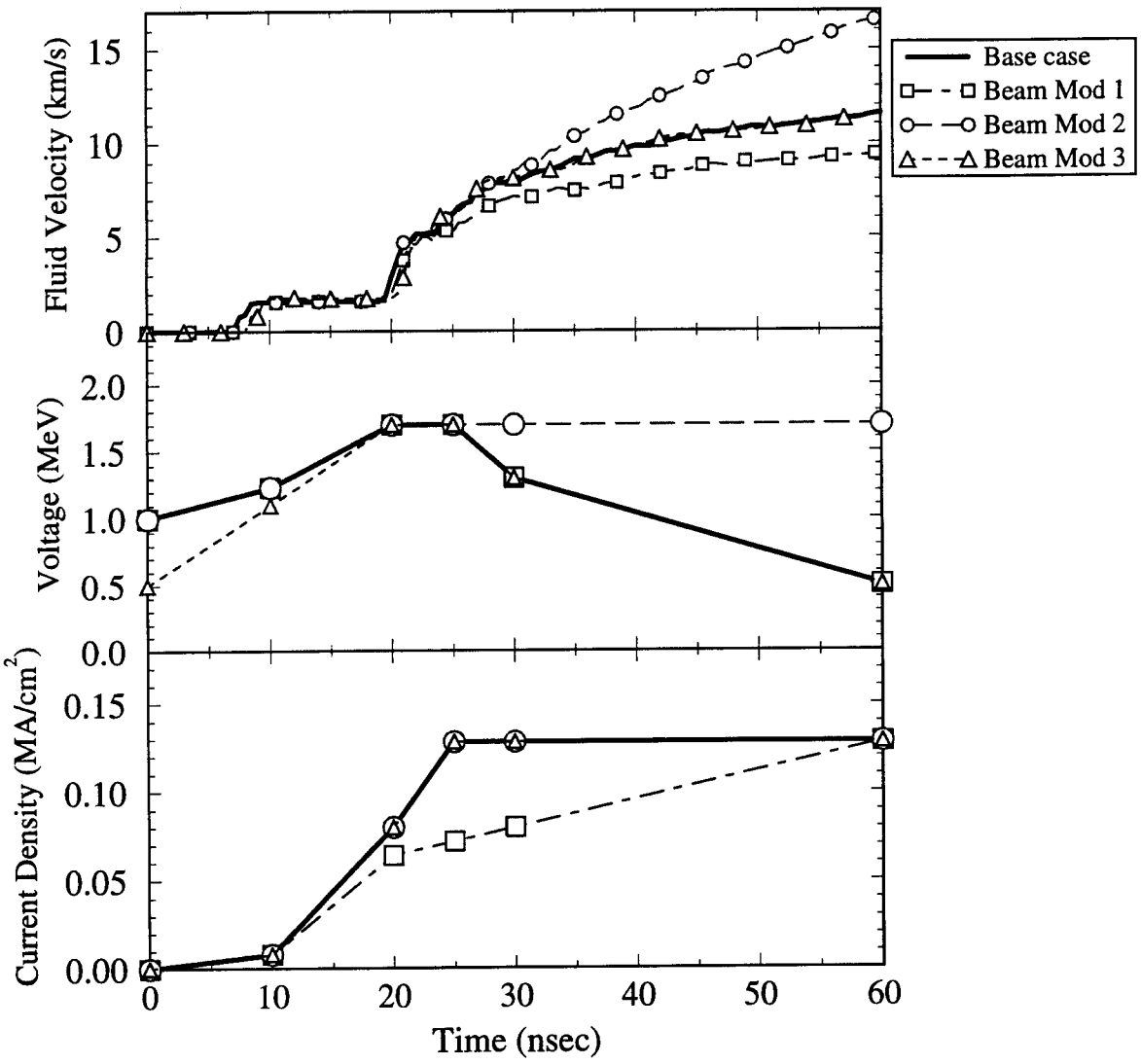

Figure 3.15. Sensitivity of calculated rear surface velocity to adjustments in the proton beam voltage and current density profiles.

4. Summary

We have presented results of simulations of KALIF shock-wave physics experiments using the applied-B diode. Results from simulations of B_θ-diode experiments were also presented to provide a comparison with previous analyses of the B_θ-diode shock-wave data. Comparisons of predictions from various EOS and stopping power models which have been used in the analysis of the KALIF experiments have also been presented.

Our results suggest that the computed rear surface velocities are quite sensitive to both the assumed EOS and the time-dependent proton beam voltage and current density. For the plasma conditions of the ion deposition region ($T \sim 1 - 10$ eV, $\rho \sim 10^{-1} - 1\,\rho_0$) EOSOPA pressures were found to be $\sim$ a few tens of percent higher than SESAME pressures, and are approximately a factor of 2 higher than those predicted by the model of Goel and Vorobjev. The higher pressures can lead to significantly higher rear surface velocities in the simulations. It was also noted that there is some dependence on the velocity with position behind the rear surface boundary. This suggests it may be important to know the depth to which the ORVIS laser light penetrates before it is reflected.

A good match to the experimentally determined rear surface velocities in the applied-B diode experiments was obtained by adjusting the time-dependent voltage and current density. The fitted beam parameters were in rough qualitative agreement with the experimentally diagnosed parameters, but there were some notable discrepancies. The fitting procedure was done while using a fixed EOS and stopping power model. Alternatively, one could hold the beam parameters fixed and adjust the EOS to match the data, as was done previously [3,4]. If the EOS of the target is well-known, the shock-wave data could in principle be used to deduce the beam parameters. On the other hand, if the beam voltage and current density profiles are accurately determined from the ion diagnostics, the target EOS can be deduced.

The sensitivity of the simulation results to the stopping power model, the use of a monoenergetic proton beam, and radiative transfer effects were also addressed. We find that radiation losses had little effect on the resultant rear surface velocity in the KALIF experiments. Also, there was only a slight change in rear surface velocity when using a multicomponent beam with a 10-20% spread in the voltage (vs. a monoenergetic beam). The velocities showed some dependence on the stopping power model, but the uncertainties introduced by this aspect of the modeling tended to be smaller than those due to the EOS or beam parameters. Similar results were obtained when using the stopping powers of Wang and Mehlhorn [13] and those of Mehlhorn [17]. Our computed ranges for protons in Al, however, were found to be $\sim 5 - 15\%$ greater than those predicted using the semi-empirical model of Polyshchuk et al. [15].

Acknowledgement

Support for this work has been provided by Forschungszentrum Karlsruhe, through Fusion Power Associates.

References

1. Baumung, K., Bluhm, H., Goel, B., Hoppe, P., Karov, H.U., Rusch, D., Fortov, V. E., Kanel, G.I., Rzaorenov, S.V., Utkin, A.V., and Vorobjev, O.Yu, "Shock-Wave Physics Experiments with High-Power Proton Beams, submitted to *Laser and Particle Beams* (1996).

2. Baumung, K., Rusch, D., Singer, J., Razorenov, S.V., Utkin, A.V., and Kauel, G.I., "Hydrodynamic Beam-Target Experiments on KALIF," in Physics of Intense Light Ion Beams and Production of High Energy Density Matter, Annual Report 1994, ed. by H. Bluhm (1995).

3. Goel, B., and Vorobjev, O.Yu, "Equation of State Information from Beam-Target Interaction Experiments at KALIF," submitted to *Laser and Particle Beams* (1996).

4. Goel, B., and Vorobjev, O.Yu, "Reinvestigation of Foil Acceleration Experiments," in Physics of Intense Light Ion Beams and Production of High Energy Density Matter, Annual Report 1994, ed. by H. Bluhm (1995).

5. "SESAME: The Los Alamos National Laboratory Equation of State Database," LANL Report LA-UR-92-3407, edited by S.P. Lyon and J.D. Johnson (1992).

6. Wang, P., "EOSOPA – A Code for Computing the Equations of State and Opacities of High Temperature Plasmas with Detailed Atomic Models," University of Wisconsin Fusion Technology Institute Report UWFDM-933 (December 1993).

7. Liberman, D.A., *Phys. Rev.* **B20**, 4981 (1979).

8. Cranfill, C.W., et al., Los Alamos National Laboratory Report LA-7313-MS (1978).

9. Feyman, R.P., Metropolis, N., and Teller, E., *Phys. Rev.* **75**, 1561 (1949).

10. Barnes, J.F., *Phys. Rev.* **153**, 269 (1966).

11. "LASL Shock Hugoniot Data," edited by Marsh, S.P. (University of California Press, Berkeley, 1980).

12. Mott, N.F., and Jones, H., "Theory of the Properties of Metals and Alloys," (Dover, New York, 1958).

13. Wang, P. and Mehlhorn, T.A., "A Unified Self-Consistent Field Model for Calculating Ion Stopping Powers in Plasmas," to be submitted to J. Appl. Phys. (1996).

14. Maynard, G., and Deutsch, C., *J. de Physique* **46**, 71 (1985).

15. Polyshchuk, A.Ya, et al., *Sov. J. Plasma Phys.* **17**, 523 (1991).

16. MacFarlane, J.J., Moses, G.A., and Peterson, R.R., "BUCKY-1 – A 1-D Radiation-Hydrodynamics Code for Simulating Inertial Confinement Fusion High Energy Density Plasmas," University of Wisconsin Fusion Technology Institute Report UWFDM-984 (August 1995).

17. Mehlhorn, T.A., *J. Appl. Phys.* **52**, 6522 (1981).